Aerospace Science and Technology 177 (2026) 112250

Contents lists available at ScienceDirect

Aerospace Science and Technology

journal homepage: www.elsevier.com/locate/aescte

Original article

Rapid preliminary aircraft wing sizing for metallic and composite structures to support data-driven multidisciplinary design optimisation frameworks

Yingjun Pan *, Mushfiqul Alam , James Whidborne , Mark Westwood

Centre of Aeronautics, Faculty of Engineering and Applied Sciences, Cranfield University, Bedford, MK43 0AL, Bedfordshire, United Kingdom

ARTICLE INFO

Communicated by Kontis Konstantinos

Keywords:
Wing sizing
Wing mass estimation
Structural analysis
Aeroelastic analysis
Multidisciplinary design optimisation
Data-driven design

ABSTRACT

To accelerate the overall design of next-generation aircraft towards Net Zero aviation, a flexible toolset of structural and aeroelastic analysis integrating multi-fidelity models within a Multidisciplinary Design Optimisation (MDO) framework has been developed. First, a discrete beam-based low-fidelity method is used to capture the dominant global behaviour of the wing, such as global stiffness and mass distribution. Second, two medium-fidelity tools, the Structural Layout Tool (SLoT) and the Structural Analysis Tool (SAIT), are used to generate parametric structural layouts and to evaluate stresses, buckling, and stiffness characteristics of semi-monocoque structures. SLoT and SAIT bridge low- and medium-fidelity methods to enable rapid and accurate sizing and optimisation, achieving computation times on the order of minutes rather than the days typically required by high-fidelity workflows at the preliminary design stage. Parametric wing box models of the NASA Common Research Model, for both composite and metallic configurations, were sized under Certification Standards CS-25 manoeuvre/gust loads, aeroelastic divergence, prescribed flutter margins, and structural safety requirements. Sensitivity analysis quantified how the design inputs (material choice, load case selection and design constraints) govern the outputs (structural mass, stiffness and aeroelastic performance). Aspect ratio and taper ratio were varied to assess transferability across wing planforms while targeting minimum structural weight subject to flutter constraints. The workflow also generated a curated dataset to support data-driven design: random-forest models with SHapley Additive exPlanations (SHAP) for feature attribution, Gaussian process regression surrogates for uncertainty-aware prediction, and an inverse-design loop for rapid design-space exploration. Findings identify the highest-leverage design inputs for reliable preliminary sizing and demonstrate a practical route to data-driven MDO with controlled accuracy and reduced computational cost.

1. Introduction

Aircraft design must satisfy strict airworthiness and certification constraints while reducing environmental impact and cost. Meeting Net Zero 2050 ambitions places greater demand on early-phase design tools to support faster decision-making and tighter performance objectives, particularly fuel burn, emissions, and noise [1–3]. Lightweight aerostructures are central to improved efficiency; however, reduced structural margins and advanced configurations–such as high-aspect-ratio wings, truss-braced concepts, and blended-wing bodies–introduce increased aeroelastic sensitivity and more demanding structural requirements. These challenges render wing design an inherently multidisciplinary task, requiring the integrated consideration of aerodynamic loads, structural layout, aeroelastic stability, manufacturability, and certification from the earliest design stages.

Industrial wing sizing progresses from low-fidelity conceptual analysis, typically using beam models for global stiffness and mass trends [4–6], to medium-fidelity preliminary design where skin-stringer or thin-wall box representations enable explicit structural layout and sizing against critical load cases [7–10]. Detailed design subsequently resolves local, part-level structural behaviour using refined three-dimensional finite element (FE) models, enabling accurate assessment of stresses, stability, and certification requirements [10–12]. Historically, preliminary sizing involved manual or rule-based iteration [13–15]. Modern programmes, however, must satisfy coupled structural, aeroelastic, cost, and environmental constraints, motivating the widespread adoption of Multidisciplinary Design Optimisation (MDO) [16].

High-fidelity MDO studies have demonstrated improved design integration, particularly when using FE-based structural models and gradient-based optimisation for large design spaces [17–20]. However, computational cost remains a major barrier. Increasing fidelity–transitioning from beam to 3D wing box models, or coupling CFD with FE–significantly increases runtime and limits the ability to explore large design spaces at preliminary timescales [6,21]. Kenway et al. [22], for

* Corresponding author.
E-mail address: y.pan@cranfield.com (Y. Pan).

https://doi.org/10.1016/j.ast.2026.112250
Received 20 January 2026; Received in revised form 18 March 2026; Accepted 28 March 2026
Available online 31 March 2026
1270-9638/© 2026 The Author(s). Published by Elsevier Masson SAS. This is an open access article under the CC BY license (http://creativecommons.org/licenses/by/4.0/).

example, reported 36 hours of wall time per optimisation using 435 processors for an aerostructural problem with 476 variables. High-fidelity MDO is therefore feasible but impractical for routine early-phase exploration where hundreds of possible design case iterations are required.

Data-driven and machine learning techniques offer opportunities to reduce evaluation cost and accelerate design iteration and have seen growing use across aerodynamics, structural health monitoring, and control [23–30]. Recent studies have begun applying AI to conceptual aircraft design; for instance, Tong et al. [31] demonstrated rapid AI-generated concepts but still relied on empirical mass models without structural layout. Hasan et al. [32] coupled low-fidelity models with machine learning surrogates to accelerate aerodynamic evaluation for box-wing configurations. These works highlight the potential of machine learning but also reveal key gaps: (i) most focus on aerodynamic prediction rather than physics-based structural sizing; (ii) structural mass is often approximated empirically; and (iii) metallic and composite wings are rarely treated within a unified framework. As a result, no existing data-driven methodology enables rapid exploration of wing configurations while capturing structural integrity, aeroelastic stability, and material-dependent sizing at preliminary-design fidelity.

The present work addresses these gaps through the development of methods that:

i. Provide flexible MDO-compatible aerostructural tools that retain essential physics, including strength and aeroelastic constraints;
ii. Enable rapid preliminary wing sizing and mass estimation for both composite and metallic structures; and
iii. Quantify the sensitivity of structural outcomes to material choice, load-case definition, and constraint formulation. The framework also generates structured datasets that support surrogate modelling and inverse design for efficient design-space exploration.

The paper is organised as follows. Section 2 describes the methodology, including the development of structural and aeroelastic tools integrated into an MDO-compatible workflow and data-driven exploration. Section 3 presents sizing results for parametric metallic and composite wing boxes based on a common reference planform, NASA Common Research Model (CRM). Section 4 reports a sensitivity study on material, load cases, and constraints. Section 5 demonstrates an MDO case with geometry and materials as design variables and uses the resulting dataset to train surrogate models for inverse design. Section 6 concludes the paper with some final remarks.

2. Methodology and procedure overview

2.1. Wing sizing methods and tools

2.1.1. Toolset overview

In earlier work, the authors developed a flexible multi-fidelity toolset for aircraft wing structural optimisation, demonstrating reductions in structural weight and improvements in flutter speed for a large composite transport-wing application [33]. As shown in Fig. 1, the toolset framework spans the full aircraft structural design process, linking low-, medium-, and high-fidelity analyses through modular blocks. The present study builds on this toolset to enable rapid preliminary design of civil aircraft structures.

Starting from conceptual design specifications for an aircraft, loading analysis identifies critical cases and derives shear, bending, and torque distributions using low-fidelity aerodynamic solvers for rapid prediction (Modules 1–2). Preliminary sizing is then performed with the medium-fidelity Structural Layout Tool (SLoT) and Structural Analysis Tool (SAIT) (Module 4) developed at Cranfield. SLoT and SAIT generate an explicit wing box structural layout based on skin-stringer panels, evaluate strength and buckling constraints, and perform static and aeroelastic analyses. A gradient-based optimisation algorithm is used to minimise structural weight subject to multiple constraints. The resulting sizing parameters can be transferred directly to a high-fidelity FE model for verification (Module 5). This workflow enables rapid preliminary design while maintaining consistency with detailed analysis, as demonstrated through cross-validation across fidelity levels [33]. Therefore, this study focuses on employing SLoT and SAIT to demonstrate a computationally efficient aerostructural MDO workflow from conceptual through preliminary design (Modules 1–4).

In addition, SLoT and SAIT support aeroelastic tailoring through laminate layup optimisation and couple to MSC NASTRAN to provide a consistent data path for higher-fidelity aeroelastic evaluation and optimisation, demonstrating flexible interoperability with external engineering software (Module 6). Detailed analyses in Modules 5–6 using high-fidelity models are beyond this manuscript's scope.

2.1.2. Aerodynamic solvers

SLoT computes aerodynamic loads for rapid structural sizing using low-fidelity methods, primarily strip theory and the ESDUpac A95010 module [34]. ESDUpac A95010 is a FORTRAN-based module that exchanges data through structured text input/output, which allows rapid update of spanwise load distributions in response to changes in wing geometry, incidence, camber, and twist during MDO iterations. Its correlation accuracy and known limitations are documented in ESDU 83040 [35]. These methods have been benchmarked against higher-fidelity solvers, including the Cranfield Viscous Full Potential (VFP) 3D solver [36] and the Athena Vortex Lattice (AVL) code [37].

2.1.3. Structural solvers

Structural design and analysis are carried out with SLoT and SAIT as summarised in Fig. 1, a suite of six in-house programs (SLoT-1–4, SAIT-1–2). The workflow comprises six stages: airframe loading, sizing, idealisation, stressing, stiffness analysis, and aeroelastic evaluation.

In this study, the wing is clamped at the root and partitioned into spanwise sections. The wing box, bounded by the front and rear spars, is treated as the primary load-carrying structure. Each section is modelled as a uniform thin-walled box beam built from stiffened skin-stringer panels. Sizing determines the panel thicknesses (skins, spar webs and rib webs), stringer dimensions, and layout needed to meet strength and buckling criteria under the applied loads. Direct stresses in stringers and shear stresses in skins are computed using thin-walled beam theory [38].

For composite panels, laminate behaviour is evaluated using classical laminate theory, which derives equivalent properties from ply material properties, ply orientations, and the laminate stacking sequence. The elastic constants E_x, E_y and G_x of the laminate are obtained, and stresses and failure indices at critical regions in the composite box beam are then assessed using thin-walled laminate theory [39].

The whole wing is modelled as an assembly of thin-walled box-beam sections. For each section, bending, torsion and bending-torsion coupling stiffness are computed using the analytical formulations of Armanios and Badir [40,41]. Vibration is analysed with the Dynamic Stiffness Matrix (DSM) method [42,43], modelling each box as a beam element and neglecting shear deformation and warping. In the DSM, each beam element relates displacements and force vectors at both ends. Assembling the element matrices along the span yields the wing's global dynamic stiffness matrix. This matrix incorporates both stiffness and mass properties and depends on frequency, leading to a non-standard eigenvalue problem. Flutter is then evaluated by the normal-mode method with unsteady aerodynamic forces from lifting-surface theory in incompressible flow; the flutter speed and frequency in the subsonic regime are obtained iteratively using the $V - g$ method [41].

All analyses are run in an automated MATLAB-based workflow, enabling rapid sizing iterations. The combined methodology allows metallic and composite wing designs to be performed efficiently at preliminary-design fidelity, delivering mass and flutter predictions while demonstrating compliance with structural and aeroelastic constraints.

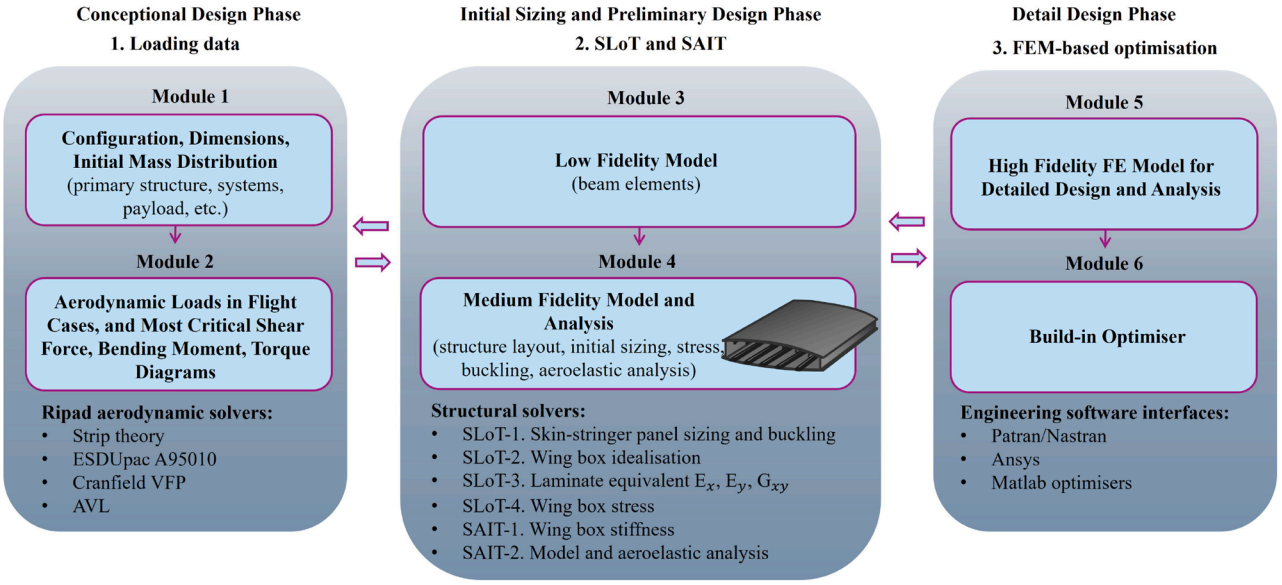


Fig. 1. Overview of a flexible multi-fidelity toolset across three design phases.

2.1.4. Structural sizing criteria

The structural design of a wing is usually determined by multidisciplinary criteria, including strength, buckling, fatigue, and aeroelastic stability, together with manufacturing constraints such as minimum stringer ratio, ply-percentage rules, and feasible laminate stacking sequences.

Strength constraints are evaluated using the maximum-stress criterion for both metallic and composite structures, together with the Tsai-Wu failure criterion for composite laminates. Compliance is assessed by monitoring the peak stresses in each panel during the sizing process. For composite panels, the stress is evaluated at the ply level in the material principal directions, and the maximum local ply stress is used for failure assessment. The reserve factor is defined as the ratio of maximum stress to allowable stress, with a design limit of 0.8 imposed in the present sizing procedure. A damage-strain tolerance limit is also enforced by requiring that the critical strain under ultimate loads remains below 3500 $\mu\varepsilon$. Buckling stability is assessed at limit load by imposing a minimum buckling factor of 1.2, defined as the ratio of critical buckling load to applied load. Buckling is assessed for both metallic and composite designs using the practical design rules of Niu [44], supplemented by the finite-strip method of ESDU 03001 for stiffened composite panels [45].

Aeroelastic stability is enforced in accordance with CS-25 requirements, which specify that the flutter speed V_f must exceed 1.15 times the dive speed V_D. Fatigue constraints are applied to the skin design using a 1.0-g cruise load case scaled by a factor of 1.3 to account for gust effects [10]. For composite designs, a reference fatigue stress limit of 1000 N/mm^2 is adopted as a preliminary design value based on published CFRP fatigue data [46,47]. For metallic designs, the corresponding limit is set at 100 N/mm^2. This value is based on the fatigue strength of aluminium alloy 7075-T6 (≈159 N/mm^2 at 5×10^8 reversed cycles), reduced to 100 N/mm^2 to account for conservative preliminary-design assumptions and structural imperfections, such as manholes and rivets.

2.2. Applied loads for wing sizing

Strength and stiffness requirements for airworthiness particularly drive wing sizing, the former governed by ground and flight loads and the latter by aeroelastic considerations. While the 2.5-g symmetric pull-up manoeuvre is often the dominant case for civil transport wing designs, additional manoeuvre, gust, landing, and engine-induced loads can generate localised critical conditions. Although industrial certification requires analysing hundreds of load cases, preliminary design typically employs a reduced set that captures the main internal load paths and distribution among the primary structural components, rather than conducting detailed local stress analysis or precise sizing of individual elements [10].

In this study, a representative subset of limit load cases is selected for preliminary sizing, including cruise, symmetric and asymmetric manoeuvres, flap-down landing loads, gust encounters, and engine-induced loads, based on CS-25 requirements and the standard transport-aircraft V–n diagram [48]. To quantify how load definition influences structural outcomes, a sensitivity study is performed in which different combinations of load cases and constraints are applied to both composite and metallic wings. The sequence of steps and associated inputs is summarised in Table 1. Aeroelastic effects are included selectively: flutter and gust response are evaluated in Step 2, and flutter is re-evaluated in Step 9 (with engine loads included) under the same 2.5-g condition for direct comparison.

2.3. Sizing objective and MDO framework

2.3.1. Sizing objective and optimisation in the SLoT–SAIT workflow

Weight reduction is a primary driver in aerostructural MDO, as structural mass directly influences fuel burn, aerodynamic performance, and operating cost. In this work, structural sizing is formulated as a constrained optimisation problem in which the total wing box weight is minimised subject to strength, buckling, fatigue, and aeroelastic constraints. Aerodynamic and structural solvers are coupled in the SLoT–SAIT workflow, and iterative sizing is performed using a gradient-based algorithm (MATLAB `fmincon`). The optimisation problem is expressed as The MathWorks, Inc. [49]:

$$\min_x f(x) \quad \text{subject to} \quad \begin{cases} c(x) \le 0, \\ ceq(x) = 0, \\ A \cdot x \le b, \\ Aeq \cdot x = beq, \\ lb \le x \le ub. \end{cases} \tag{1}$$

where x contains the design variables (skin and spar-web thicknesses, stringer sizing parameters); $f(x)$ is the objective function to be

Table 1
Design load cases and constraints for sensitivity analysis.

Step	Load case and description	Design constraints
1	2.5-g symmetric pull-up at sea level, without inertial loads	Strength (stress-based)
2	2.5-g symmetric pull-up at sea level, without inertial loads	Strength + buckling + aeroelastic
3	2.5-g symmetric pull-up at sea level, add wing box inertial loads	Strength + buckling
4	2.5-g symmetric pull-up at sea level, add inertial loads of wing box, LE & TE and fuel tank	Strength + buckling
5	1.0-g symmetric at sea level with 1.3 load factor for fatigue	Strength + buckling + fatigue
6	−1.0-g symmetric push-down at sea level	Strength + buckling
7	2.0-g flap down at sea level	Strength + buckling
8	Critical rolling manoeuvre loads at sea level	Strength + buckling
9	Critical engine loads with 2.5-g load	Strength + buckling + aeroelastic

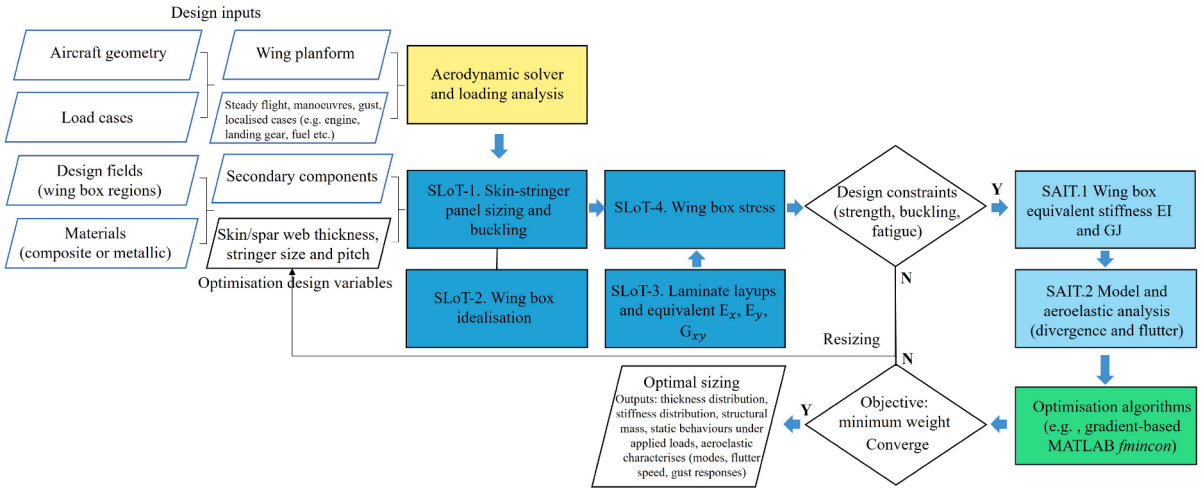


Fig. 2. MDO sizing workflow.

minimised, i.e., the total wing box weight; $c(x)$, $ceq(x)$ are nonlinear constraint functions; A, Aeq define linear constraint functions; lb, ub are variable bounds. The constraint functions implement the structural and aeroelastic requirements in Section 2.1.4, evaluated under the load cases in Table 1.

2.3.2. MDO Sizing process overview

The wing sizing workflow within the MDO framework is illustrated in Fig. 2. It extends the SLoT–SAIT process to accommodate multiple design variable settings. Key inputs include aircraft data, load cases, wing planform, material system, wing box design fields, and secondary wing components. Each design loop yields an optimised wing structural layout and sizing, with detailed outputs: component thicknesses, spanwise mass and stiffness distributions, static behaviours under the applied loads, and aeroelastic characteristics (mode shapes and frequencies, flutter speed, and gust response).

To maintain computational efficiency for many design evaluations, aerostructural coupling, where wing deformation alters aerodynamic loads, is not fully modelled. Therefore, the workflow runs open loop: structural sizing is driven by prescribed loads without iterative aerodynamic updates. Despite this simplification, the sensitivity study in Table 1 still reveals the influence of different load cases and constraints on sizing trends, particularly for local load-driven effects such as pylon/engine-induced loads and stiffness-induced load redistribution. In parallel, the jig shape is derived from the aircraft design flight shape at the nominated cruise condition, which implicitly incorporates the flexible-wing aeroelastic characteristics of the intended operating condition. This avoids the rigid-wing assumption while eliminating the computational cost of a fully coupled aeroelastic loop, preserving fidelity appropriate for preliminary MDO studies.

Using a common reference planform, modelling fidelity and tool capability are assessed by varying (i) design inputs (representative load cases); (ii) airworthiness-driven constraints (strength, buckling, stiffness, aeroelastic margins); (iii) material system (metallic versus composite); and (iv) model resolution (wing-section discretisation). These variations produce distinct sizing outcomes. These variations produce distinct sizing outcomes. Their effects on structural mass, static deformation, and aeroelastic performance are quantified in the sensitivity analysis of Section 4. The results then guide the selection of variables and constraints for the Section 5 studies (MDO with varying wing planforms and data-driven exploration).

2.4. Machine learning models for data-driven exploration

2.4.1. SHAP analysis for feature importance and sensitivity

SHapley Additive exPlanations (also known as SHAP) is a model-agnostic method that attributes the difference between a sample's prediction and the dataset mean to individual input features, yielding additive contribution values for each feature [50–52]. It is particularly effective for ensemble tree models such as Random Forest (RF) [53] and XGBoost [54], for which SHAP values can be computed efficiently. In this study, SHAP is used to interpret the machine learning predictions of wing mass and flutter speed and to relate these attributions to the earlier sensitivity analyses performed with the toolset.

To model the effects of geometric parameters and material system on the wing sizing, an RF regression model [53] was trained separately for each output (mass and flutter speed). RF is an ensemble of decision trees that combines multiple bootstrapped learners to approximate nonlinear, multi-factor relationships without assuming an explicit analytical form. The input feature vector x comprises the design variables aspect ratio (AR), taper ratio (TR), span, and material type. The RF prediction for a given design x, denoted $\hat{y}(x)$, is the estimated wing mass or flutter speed and is computed as

$$\hat{y}(x) = \frac{1}{N_t} \sum_{i=1}^{N_t} f_i(x) \tag{2}$$

where $f_i(x)$ denotes the i^{th} decision tree and N_t is the number of trees in the ensemble.

Feature importance and sensitivity are then quantified by analysing the trained RF models with the TreeSHAP algorithm in Python [50,55]. TreeSHAP computes exact SHAP values for tree ensembles in polynomial time and decomposes each prediction $y(x)$ into a baseline (the mean model output) plus a sum of feature contributions:

$$\hat{y}(x) = E[\hat{y}] + \sum_j \phi_j(x) \tag{3}$$

where $E[\hat{y}]$ is the mean model output and $\phi_j(x)$ is the SHAP value of feature j, measuring its marginal impact on the prediction relative to this baseline.

Therefore, SHAP values provide a complementary interpretability layer. Globally, they quantify feature importance through the average magnitude of each feature's contribution; locally, they describe how each feature influences an individual prediction.

2.4.2. Gaussian process regression (GPR) for uncertainty-aware design

Gaussian Process Regression (GPR) [56] was employed as a probabilistic surrogate model to predict wing mass and flutter speed, providing both mean estimates and associated uncertainties for each design. GPR is a Bayesian non-parametric approach in which the latent function $f(x)$ is modelled as a realisation of a Gaussian process [56,57],

$$f(x) \sim \mathcal{GP}\big(m(x),\ k(x,x')\big) \tag{4}$$

where $m(x)$ is the mean function (set to zero) and $k(x,x')$ is a positive-definite covariance (kernel) function that encodes spatial smoothness and correlation.

In this study, a radial basis function kernel was used to capture smooth geometric trends, combined with a WhiteKernel term to represent numerical and measurement noise [56]. The training inputs $X = \{x_i\}_{i=1}^n$ (including AR, TR, span, and one-hot-encoded material type) were processed through a scikit-learn pipeline [58] before fitting the GPR model. The corresponding outputs $\mathbf{y} = [y_1, \dots, y_n]^\top$ (e.g. wing mass or flutter speed), standard GPR assumes $\mathbf{y} \sim \mathcal{N}(0, K(X,X) + \sigma_n^2 I)$, where $K(X,X)$ is the kernel matrix and $\sigma_n^2 I$ is the noise variance.

For a new design point x^*, the GP posterior distribution is Gaussian,

$$f(x^*) \mid X, \mathbf{y} \sim \mathcal{N}(\mu(x^*), \sigma^2(x^*)) \tag{5}$$

where $\mu(x^*)$ and variance $\sigma^2(x^*)$ denote the predictive mean and variance, respectively [56]. From this Gaussian predictive distribution, confidence intervals are obtained as $\mu(x^*) \pm z\sigma(x^*)$ where z is the critical value of the standard normal distribution corresponding to the desired coverage probability. In particular, a two-sided 95% prediction interval for the model response is given by $\mathrm{PI}_{95\%}(x^*) = \mu(x^*) \pm 1.96\sigma(x^*)$ following the standard normal-approximation convention [59]. These intervals distinguish designs that are deterministically feasible from those robustly feasible under model uncertainty (chance-constraint interpretation). A Leave-One-Out (LOO) validation was additionally performed to evaluate model generalisation given the limited dataset.

2.4.3. Inverse design using the data-driven surrogate models

To demonstrate design synthesis from the trained surrogates, an inverse design problem was formulated to identify wing configurations that minimise structural mass while satisfying prescribed flutter requirements. The design vector x = AR, TR, span, material was constrained within the bounds of the original dataset, and the RF surrogate $\hat{m}(x)$ was used as an objective for mass. Flutter was treated as a constraint using the GPR surrogate $\mu_F(x)$ and $\sigma_F(x)$, and only designs whose predicted flutter speed exceeded a target value $F_{\min}$ of 250 m/s with high confidence were retained.

A simple Monte Carlo search [60,61], based on uniform random sampling of the design space, was adopted instead of gradient-based optimisation because of the discrete material variable and non-smooth ensemble surrogates. A large set of candidate designs was sampled uniformly in the admissible space, evaluated with the surrogates, and retained only if they satisfied (i) a deterministic constraint $\hat{F}(x) \geq F_{\min}$ and (ii) a chance constraint based on the 95% one-sided lower confidence bound $L(x) = \mu_F(x) - 1.96\sigma_F(x) \geq F_{\min}$ on flutter speed. The feasible designs were then ranked by $\hat{m}(x)$ and a small set of lowest-mass candidates was reported. Additionally, "paired" designs with identical AR, TR, and span but different materials were generated to enable direct material comparisons.

In summary, surrogates trained on the toolset-generated dataset enable interpretable, uncertainty-aware inverse design, yielding low-mass wing configurations that satisfy multiple constraints and reveal material trade-offs. This capability accelerates early-stage MDO and is readily extensible to broader variables and objectives.

Table 2
Aircraft specifications.

Parameter	Value	Parameter	Value
Wing AR	9	Maximum take-off weight (MTOW, kg)	297 500
Wing reference surface area (m^2)	383.69	Maximum landing weight (MLW, kg)	213 180
Wing semi-span (m)	29.38	Maximum zero fuel weight (MZFW, kg)	195 040
Mean aerodynamic chord (m)	7.01	Operational empty weight (OEW, kg)	138 100
Quarter-chord sweep angle (°)	35	Reserve fuel (kg)	15 000
Cruise Mach number	0.85	Engine mass (kg)	7 320
Cruise lift coefficient	0.5	Takeoff thrust (kN)	417
Initial cruise altitude (ft)	37 000	Maximum cruise thrust (kN)	95

3. Aircraft data and wing sizing under the standard 2.5-g load case

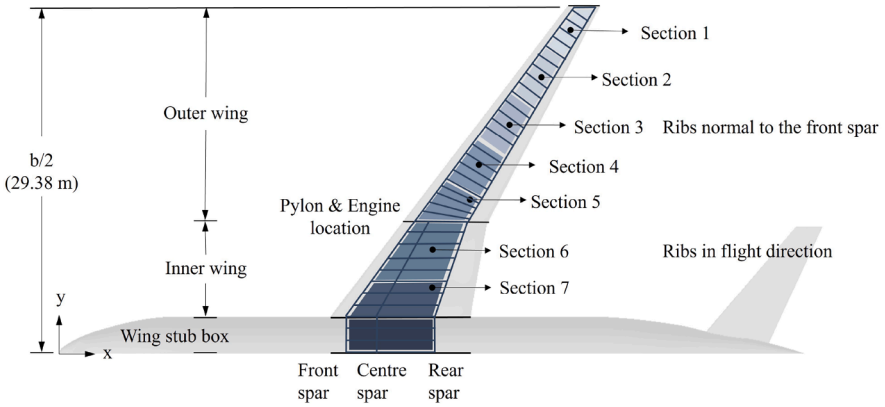
3.1. Aircraft data

The NASA Common Research Model (CRM) is used as the reference configuration for this study. Since its introduction through the Drag Prediction Workshop series, the CRM has become a widely adopted benchmark in CFD research and is frequently used for verification and validation, often alongside wind-tunnel experiments and aerodynamic shape optimisation studies [26,62–64]. The CRM represents a long-range, twin-aisle transport aircraft and includes a fuselage, wing, horizontal tailplane, and engine nacelles with pylons. Key geometric parameters are summarised in Table 2, with selected values referenced from the Boeing 777-200ER due to its close similarity to the CRM configuration [65].

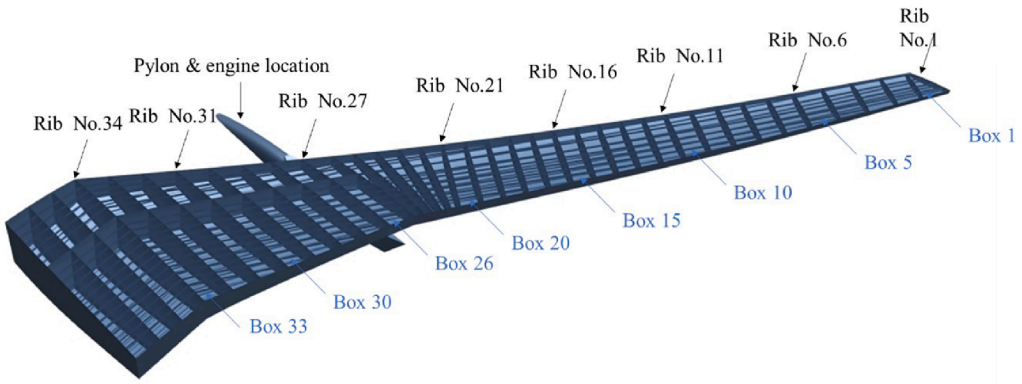
3.2. Wing sizing models

The structural layout comprises the outer wing, the inner wing, and the wing stub box attached to the fuselage, as shown in Fig. 3. Design and optimisation activities focus on the inner and outer wing sections, which form the primary load-carrying structure. This structure consists of stiffened upper and lower covers, subdivided into 33 wing boxes from tip to root according to rib positions, with rib spacing varying across the span.

Structural sizing is performed at two modelling resolutions: a 7-section model and dummyTXdummy– a 33-section model. In the 7-section model, the wing is grouped into larger regions with uniform panel thicknesses and stringer dimensions within each section (Fig. 3a): Section 1, Boxes 1–5; Section 2, 6–10; Section 3, 11–15; Section 4, 16–20; Section 5, 21–26; Section 6, 27–30; Section 7: 31–33). In the 33-section model, each wing box segment between adjacent ribs is explicitly represented and independently sized (Fig. 3b). Sizing is carried out section by section to minimise structural mass under the selected load cases and constraints. Using identical loading and constraint sets



(a) Wing discretised into seven aggregated sections (7-section model)



(b) Wing box layout with 33 rib-bay boxes (33-section model)

Fig. 3. Wing-box structural layout and discretisation.

Table 3
Material properties of structural components.

Wing model/components	Material	Density (kg/m^3)	E/E_1 (GPa)	E_2 (GPa)	G/G_{12} (GPa)	ν/ν_{12}
Metallic model – whole wing; Composite model – spar caps, stringers, rib flange, web stiffeners	Aluminium alloy	2810	71.7	–	26.9	0.33
Composite model – skin covers, spar, rib webs	Composite laminate	1586	176	15.6	5.6	0.27

across both resolutions enables assessment of how modelling fidelity influences mass prediction and structural response.

In the outer wing, the front and rear spars are located at 11% and 70% of the local chord. In the inner wing, spars are positioned at 10%, 31% and 70% of the chord, with ribs oriented normal to the front spar. The pylon and engine are mounted at the wing kink (Rib No. 27). Cut-outs in spars and rib webs, as well as manholes in the lower skin, are omitted from the present model, as their influence on global stiffness and load distribution is negligible at the fidelity level required for preliminary MDO analysis.

The material properties are summarised in Table 3. For the composite wing design, an intermediate modulus carbon/epoxy prepreg (M91/IM10UD) is applied to skin and web panel elements. The material is characterised by modulus E_1 and strength X_t and X_c in the fibre direction, modulus E_2 and strength Y_t and Y_c in the off-fibre direction, and shear modulus G_{12} and strength S. The initial composite layout adopts a quasi-isotropic laminate with ply percentages of (50/40/10), following established design guidelines and manufacturing constraints. For both composite and metallic designs, spar caps, stringers, rib flanges, and web stiffeners are modelled using aluminium alloys with T-shaped cross-sections. Their dimensions follow practical design rules and buckling guidelines provided by Niu [44].

The mass of secondary structures is estimated using empirical methods [10,66], as illustrated in Fig. 4. Mass distribution is calculated from the projected areas of secondary components and fuel tanks and represented within the SLoT framework as lumped masses distributed along the front and rear spars. The arrangement of secondary structures and fuel tanks is shown in Fig. 5. The maximum fuel weight is approximately 125,400 kg, with about 60% stored in the wing tanks and the remaining 40% in the centre fuselage tank.

3.3. Sizing process

This section focuses on the standard 2.5-g symmetric pull-up at sea level with strength, buckling, and aeroelastic constraints (Step 2 in Table 1). The aim is to establish baseline sizing solutions and demonstrate the workflow capabilities, including panel-thickness optimisation, mass estimation, static deformation and jig-shape prediction, and aeroelastic assessment.

Beyond loads, constraints, and material systems, stringer sizing and pitch are treated as key design variables. Both uniform and spanwise-varying pitch distributions are examined to evaluate their influence on skin–stringer panel design and mass. Comparative results for composite

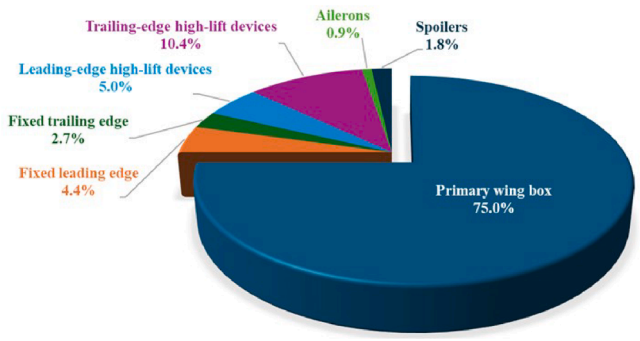


Fig. 4. Mass breakdown of the wing structure.

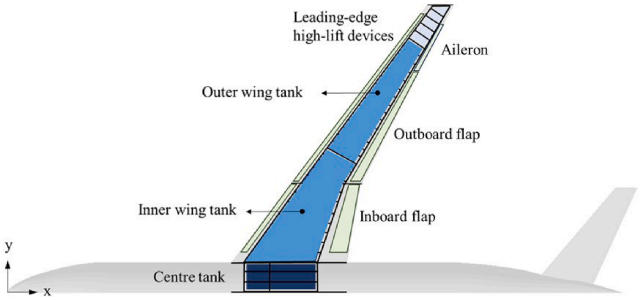


Fig. 5. Schematic layout of secondary structures and fuel tanks.

and metallic wings are then presented to highlight how material choice affects structural weight and behaviour at the two modelling resolutions.

Fig. 6 illustrates the outcome of the automated sizing optimisation process outlined in Fig. 2. In the composite case (Fig. 6a), symmetric laminate configurations are assumed, with the design variables defined as the semi-laminate ply counts for the upper skin, lower skin, front spar, and rear spar (variables 1–4). In the metallic case (Fig. 6b), the corresponding design variables are the panel thicknesses of these same structural components. For multi-cell wing box configurations, additional structural elements are introduced and numbered sequentially (for example, the middle spar is defined as variable 5).

The function-evaluation trace records the number of calls to the coupled SLoT/SAIT analysis, the function-value trace shows the evolution of the objective function (wing box mass), and the constraint-violation trace monitors satisfaction of the imposed structural constraints, where a value of zero indicates that all strength and stiffness requirements are met. The optimisation process proceeds until convergence is achieved, resulting in the final optimised component sizing.

The wall-clock time required for a complete optimisation run depends on several factors, including the material system, the number of active design fields, the bounds placed on the design variables, and the optimisation algorithm settings. In Fig. 6, results for Box 1 are compared for composite and metallic configurations under identical loading conditions and optimisation settings, with convergence declared when the step-size, constraint, and optimality tolerances satisfied tolerances of 10^{-6}.

Composite sizing generally requires longer runtimes than the metallic case due to the additional laminate analysis and the associated increase in function evaluations. Nevertheless, the sizing of a wing box can typically be completed on the order of minutes, representing a substantial reduction in computational effort compared with full finite element model generation and coupled CFD-based analysis. This efficiency enables rapid exploration of the design space during preliminary-stage MDO.

Table 4
Total mass results of the sized wing models obtained from the 2.5-g load case.

Stringer configuration	Material	Design models	Total mass (kg)
Variable pitch	Composite	7-section	8172.34
		33-section	8088.24
	Metallic	7-section	11694.75
		33-section	10682.23
Uniform pitch	Composite	33-section	6835.99
	Metallic	33-section	15601.96

3.4. Sizing results

Fig. 7 summarises the sizing results for the composite and metallic wing configurations, presenting spanwise thickness distributions for the upper and lower skins, front and rear spars, and middle spar, together with the corresponding sectional mass distribution from the wing tip (Box 1) to the root (Box 33).

As illustrated in Fig. 7a–f, the 7-section model exhibits a stepwise thickness distribution, which arises from the assumption of uniform sizing within each design section. In contrast, the 33-section model produces smoother but more locally varying thickness profiles, with clearer differentiation between skins and spars. This behaviour reflects the finer spanwise discretisation, which allows the optimiser to respond more directly to local load variations and structural constraints.

In the 33-section model, each box is sized independently, resulting in noticeable thickness changes between adjacent sections–particularly in the lower skin and rear spar–where neighbouring sections may converge to different local optima. By comparison, the 7-section model enforces a single thickness value within each design region, such that sizing is governed by the most critical subsection within that region, leading to more uniform but potentially conservative thickness distributions.

Fig. 7 also compares designs obtained using uniform and variable stringer sizing strategies. For the metallic wing, adopting a uniform stringer pitch reduces mass in the outer wing but leads to a substantial mass increase in the inner wing. This occurs because, under high shear loads near the root, both panel thickness and the total number of stringers must increase simultaneously to satisfy buckling constraints. In contrast, variable stringer sizing allows the pitch to adapt locally to the loading environment, enabling reductions in panel thickness without a disproportionate increase in stringer count, thereby yielding a lighter and more structurally efficient layout.

A similar trend is observed for the composite wings. Uniform stringer sizing permits thinner panels but increases the overall mass due to the higher stringer count associated with a smaller pitch. However, owing to the higher strength and buckling resistance of composite laminates, the composite wing does not require the same degree of inner-wing thickness increase as the metallic configuration to satisfy shear and buckling constraints. These results illustrate the inherent trade-off between buckling resistance and structural mass in skin-stringer panels and emphasise the importance of jointly optimising panel thickness and stringer pitch in lightweight wing design.

The total wing masses derived from the sectional mass distributions are summarised in Table 4. Among the configurations considered, the metallic wing with uniform stringer sizing is the heaviest, primarily due to increased inner-wing thickness and a high stringer count. The composite wing with uniform stringers is the lightest configuration, benefiting from higher laminate strength despite the increased number of stringers. Nevertheless, the use of thinner composite panels may reduce global stiffness and introduce potential aeroelastic penalties, which are examined in the subsequent sections. Overall, the composite configurations achieve an approximate 30% reduction in mass relative to the corresponding metallic designs.

The total mass predictions obtained from the 7-section and 33-section models differ by approximately 1% for the composite wing and

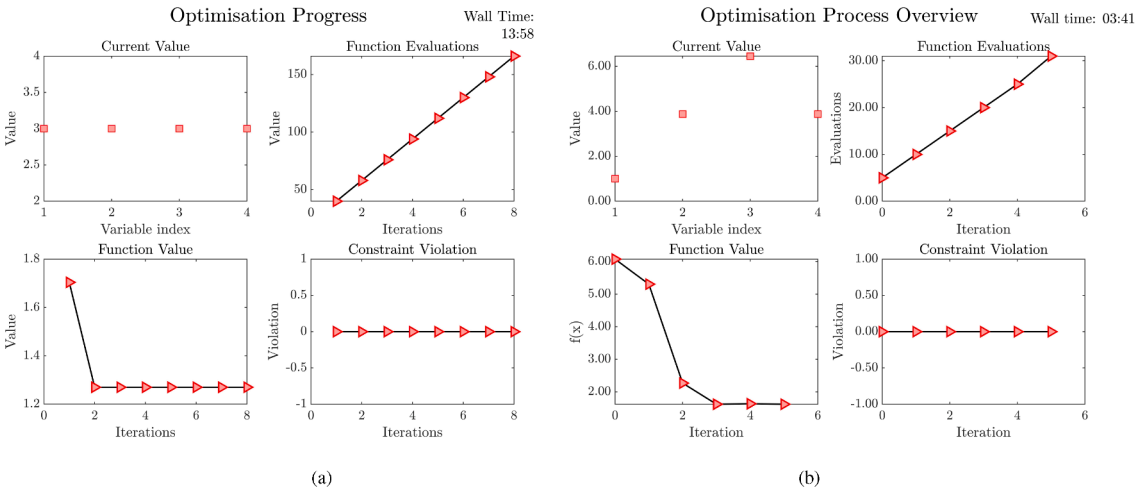


Fig. 6. Sizing optimisation process for a single-cell (a) composite wing box and (b) metallic wing box.

Table 5
Wingtip deflection and elastic twist angle of the sized wing models under the 2.5-g load.

Stringer configuration	Material	Design models	Wingtip deflection (m)	Wingtip twist angle (°)
Variable pitch	Composite	7-section	0.75	3.17
		33-section	0.76	3.68
	Metallic	7-section	0.94	4.51
		33-section	1.01	4.39
Uniform pitch	Composite	33-section	3.02	12.29
	Metallic	33-section	3.50	11.39

8.6% for the metallic wing. Coarser discretisation can lead to conservative mass estimates, whereas finer discretisation may introduce local thickness variations that complicate manufacturing considerations. Both discretisation levels capture the dominant loading trends along the span, and despite differences in local thickness distributions, the resulting total mass estimates are sufficiently close to justify the use of either model in the subsequent sensitivity analyses.

3.5. Static aeroelastic behaviour

The static aeroelastic response of the sized wings under the 2.5-g symmetric sea-level load case is evaluated using the box-element models and characterised in terms of spanwise deflection and elastic twist. The corresponding wingtip deflections and twist angles are summarised in Table 5. Configurations employing variable stringer pitch exhibit noticeably smaller deflections and twist angles than their uniform-pitch counterparts, reflecting the higher bending and torsional stiffness achieved through locally adapted structural layouts. In contrast, uniform-pitch configurations show larger elastic twist magnitudes, which may increase susceptibility to torsional divergence under static loading. On this basis, subsequent analyses focus on the variable-pitch configurations, which provide improved static aeroelastic performance while maintaining structural efficiency.

Fig. 8 presents the spanwise deflection and elastic twist distributions for the variable-pitch wing configurations. The refined 33-section model exhibits a smoother spanwise stiffness distribution and a slightly steeper deformation gradient, indicating a reduction in discretisation-related artefacts compared with the coarser 7-section model.

For the composite wing, the predicted tip deflections are nearly identical between the 7- and 33-section models (0.75 m and 0.76 m, respectively). However, the 33-section model yields a larger tip twist (3.68° compared with 3.17°), suggesting a reduction in effective torsional stiffness resulting from more localised thickness and stiffness variations. In contrast, the metallic wing exhibits a slightly smaller tip twist in the 33-section model, indicating a different sensitivity to spanwise discretisation. These observations highlight that modelling resolution influences composite and metallic designs differently through its effect on local stiffness distribution.

When comparing material systems, the composite wings consistently exhibit lower deflection and elastic twist than their metallic counterparts, reflecting the higher stiffness-to-weight efficiency achieved in the optimised composite configurations. The nonlinear deformation profiles shown in Fig. 8 also indicate partial suppression of wingtip deformation in the composite case, underscoring the role of laminate tailoring in shaping spanwise stiffness distribution and governing the static aeroelastic response.

3.6. Jig shape estimation

The jig shape is the undeformed, manufactured shape of the wing structure. It is defined such that, after aeroelastic deformation under the nominal cruise load, the wing attains the intended aerodynamic flight shape. Therefore, the jig shape compensates for bending and twist occurring in operation and is an essential output of preliminary wing sizing.

The jig shape is estimated by analysing the elastic deformation of the sized wings under the nominal 1-g level-flight condition at 37 000 ft, $M = 0.85$, and $C_L = 0.5$. Using the 33-section composite and dummyTXdummy– metallic models with variable-stringer configurations, the jig twist distribution is obtained by subtracting the elastic twist from the CRM design flight shape. The resulting jig and corresponding flight shapes are shown in Fig. 9. Under 1-g loading, the computed wingtip deflections are 0.22 m for the composite wing and 0.29 m for the metallic wing.

3.7. Modal and flutter analysis

The first five vibration modes of the sized wings were computed using SAIT and subsequently used as inputs for flutter prediction. The resulting natural frequencies and flutter speeds are summarised in Table 6.

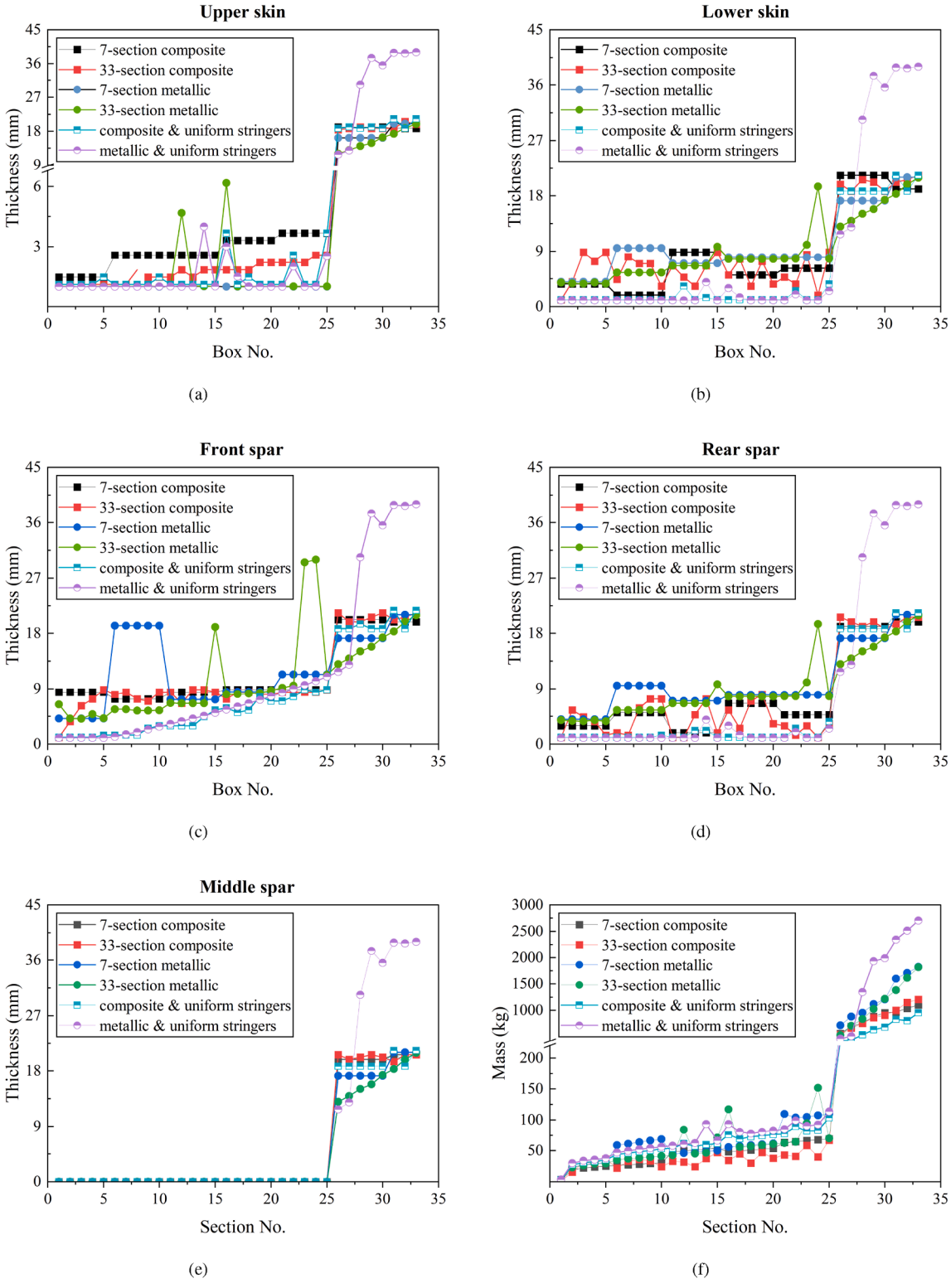
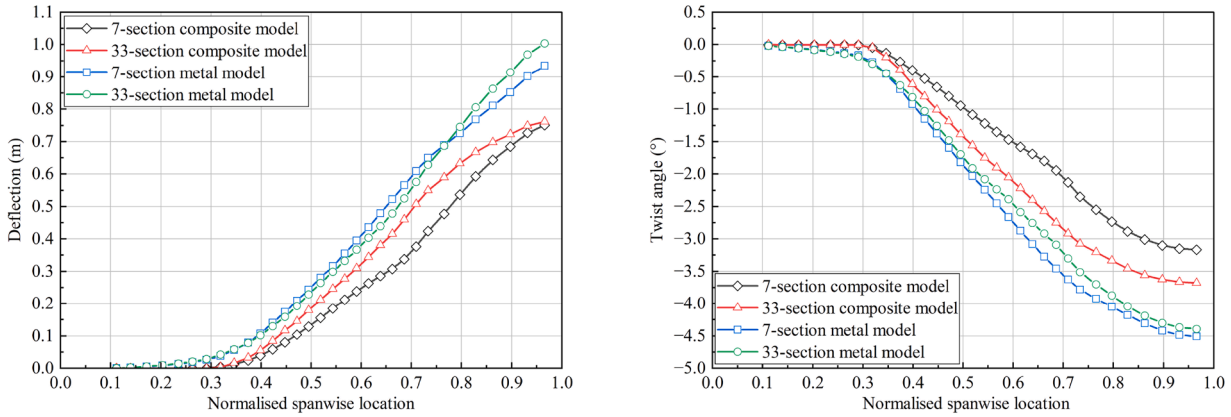


Fig. 7. Spanwise sizing results for composite and metallic wings obtained using coarse 7-section and refined 33-section models under the 2.5-g load case.

In all configurations considered, the critical flutter mechanism is associated with bending-torsion coupling between Modes 4 and 5. No flutter onset was identified within the investigated sea-level flight envelope.

Uniform-stringer configurations exhibit noticeably lower flutter speeds than the corresponding variable-stringer designs. This behaviour reflects their reduced bending and torsional stiffness, which places them closer to aeroelastic stability margins. In contrast, variable stringer sizing provides increased stiffness where required, resulting in a more robust aeroelastic response and improved suitability for MDO within the proposed framework.

The refined 33-section models predict lower flutter speeds than the coarser 7-section models, consistent with the finer spanwise discretisation capturing local stiffness reductions introduced during optimisation. When comparing material systems, the metallic wings achieve slightly



(a) (b)

Fig. 8. (a) Spanwise deflection and (b) elastic twist of the sized wings with variable stringer pitch under the 2.5-g load.

Table 6
Mode frequencies and flutter results at sea level of the sized wings.

Modal Descriptions	Mode 1 (Hz)	Mode 2 (Hz)	Mode 3 (Hz)	Mode 4 (Hz)	Mode 5 (Hz)	Flutter speed (m/s)	Flutter frequency (Hz)
7-section composite	2.65	9.82	23.59	43.62	73.85	627.50	50.03
33-section composite	2.89	10.91	23.97	44.15	77.77	548.50	59.27
7-section metallic	2.58	11.72	28.19	52.33	87.75	637.50	64.34
33-section metallic	2.58	9.16	24.09	45.27	75.41	594.50	57.55
33-section composite with uniform stringers	1.03	3.80	10.17	19.87	30.80	298.00	21.69
33-section metallic with uniform stringers	0.87	3.09	7.54	10.75	17.96	257.50	15.27

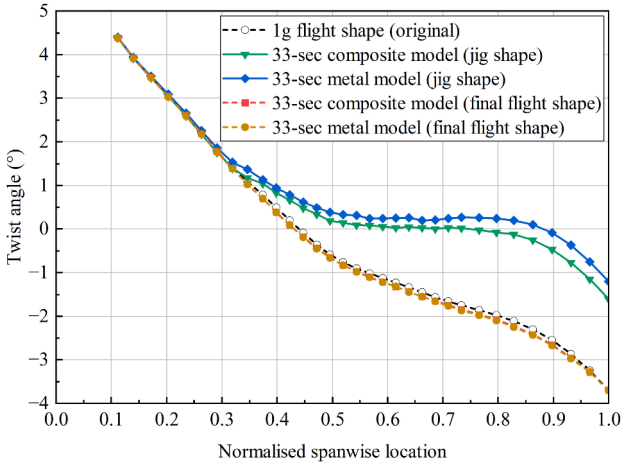


Fig. 9. Estimated jig shapes and 1-g flight shapes of the sized wings, compared with the CRM design flight shape.

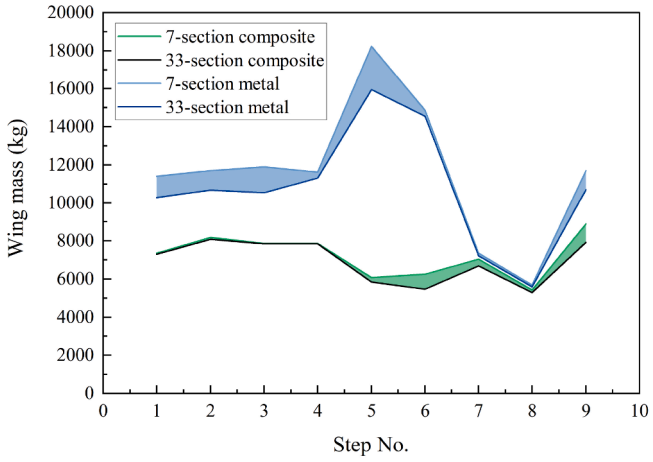


Fig. 10. Comparison of wing mass predictions from 7-section and 33-section models for composite and metallic wings across the sensitivity-analysis steps.

higher flutter speeds but require approximately 30% greater structural mass (Table 4) to do so. These results highlight the advantage of composite laminates, whose high specific stiffness and tailoring capability enable lighter designs while maintaining favourable aeroelastic behaviour relative to conventional metallic structures.

4. Importance and sensitivity of key design inputs

4.1. Effects of load cases and constraints on mass estimation

Fig. 10 compares the wing masses obtained from the 7-section and 33-section models for both composite and metallic configurations across the sensitivity-analysis steps defined in Table 1. The influence of spanwise discretisation is clearly evident. For the composite wing, the mass difference between the two discretisation levels remains small under the dominant 2.5-g loading condition (Steps 1–4) and begins to diverge after Step 5, when additional manoeuvre load cases and the fatigue constraint are introduced. In contrast, the metallic wing exhibits greater sensitivity to model resolution across Steps 1–6, with a maximum mass discrepancy of approximately 12%.

From Step 1 to Step 4, mass growth is driven primarily by the introduction of buckling constraints and inertial loading. Buckling has a pronounced influence on the composite wing, increasing mass by approximately 11% between Steps 1 and 2 as laminate thicknesses increase to resist shear stresses. In contrast, the metallic wing exhibits a more modest mass increase of about 2.5%, indicating that its sizing is governed more strongly by localised load effects associated with secondary structural components than by global buckling constraints.

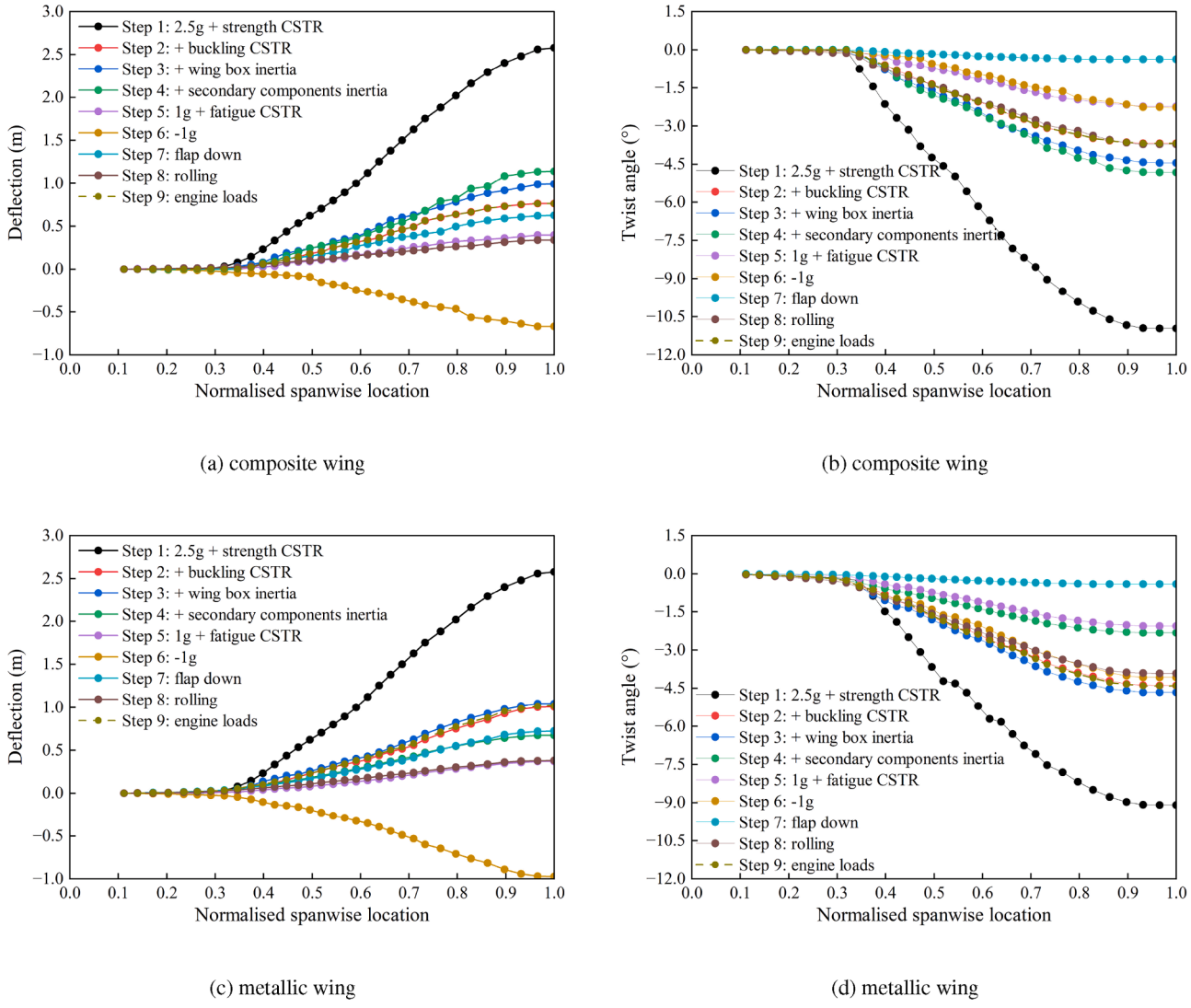


Fig. 11. Spanwise distributions of structural behaviour for the 33-section model across all steps of the sensitivity analysis: (a) deflection and (b) twist angle of the composite wing; (c) deflection and (d) twist angle of the metallic wing.

Between Steps 5 and 8, composite wing sizing becomes increasingly sensitive to the magnitude of the applied loads. Reducing the load factor from 2.5 to 1 g leads to a significant mass reduction at Steps 5/6, after which the refined 33-section model begins to outperform the coarse model by enabling additional thinning of lower-skin panels and localised modifications around trailing-edge devices. By contrast, the metallic wing exhibits a marked mass increase at Steps 5/6. This behaviour reflects the comparatively lower fatigue strength of metallic materials, whereas composite laminates can sustain reduced thicknesses under fatigue-driven constraints.

At Step 9, engine loads–including vertical inertial forces and thrust–are converted into equivalent internal shear forces and applied under the 2.5-g condition. These loads act locally near the engine attachment regions and increase stress levels in both material systems. In the 7-section model, the coarse discretisation enforces uniform thickening over relatively large regions, resulting in a noticeable mass increase. The 33-section model, however, captures the localised nature of the engine-induced load paths more accurately and maintains a total mass comparable to that obtained at Step 4. This result demonstrates that finer spanwise discretisation is important for representing engine-driven loads without introducing artificially conservative global mass penalties. The associated aeroelastic implications of engine loads are discussed in Section 4.3.

4.2. *Effects of load cases and constraints on structural behaviour*

Fig. 11 presents the spanwise deflection and elastic twist distributions for the refined 33-section models across all steps of the sensitivity analysis. The composite and metallic wings exhibit distinct stiffness responses, reflecting differences in material properties and the resulting sizing outcomes under each combination of loads and constraints. The baseline 2.5-g stress-only condition (Step 1) produces the largest overall deflections and elastic twists. In subsequent steps, the wings generally exhibit increased stiffness and reduced deformation as additional constraints and load cases are introduced. This trend indicates that the progressive inclusion of key design inputs leads to structurally stiffer configurations and improved global load-carrying efficiency.

To quantify these trends, Fig. 12 shows wingtip deflection and twist together with the percentage change relative to Step 1 for each material. Let y_1 and y_i denote the values at Step 1 and Step i, respectively. The percentage change is defined by

$$\Delta_i(\%) = \frac{y_1 - y_i}{y_1} \times 100 \tag{6}$$

Under the same 2.5-g loading condition across Steps 1–4, the composite wing exhibits its largest stiffness increase at Step 2, indicating that buckling constraints are a dominant driver of global structural be-

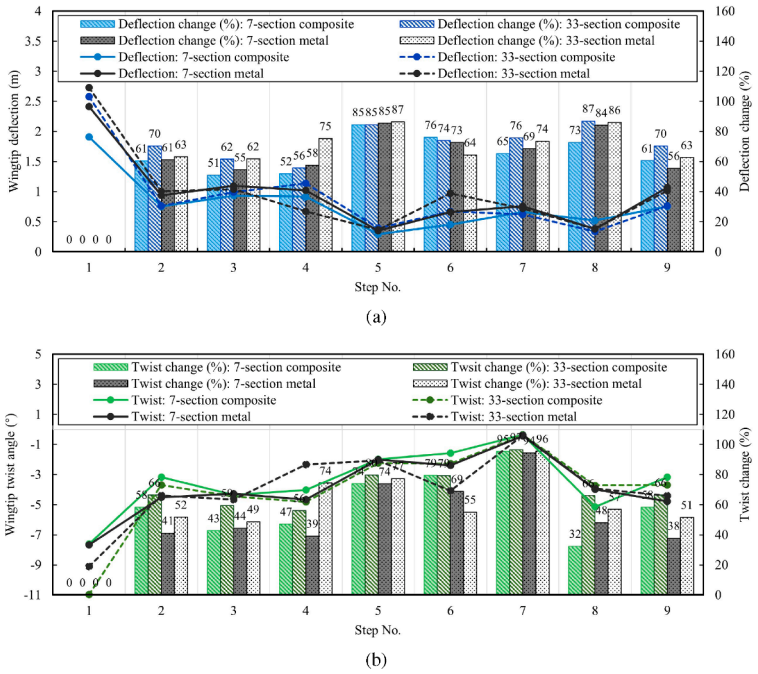


Fig. 12. (a) Wingtip deflection and (b) twist angle with percentage changes across the sensitivity analysis steps.

haviour. Relative to Step 1, bending stiffness increases by 61% and 70% in the 7- and 33-section models, respectively, while torsional stiffness increases by 58% and 66%. This response reflects the need for increased laminate thickness to satisfy shear-driven buckling requirements, which strongly influence the global stiffness distribution in composite wings.

For the metallic wing, the stiffness response differs between discretisation levels. The 7-section model shows relatively small changes across Steps 1–4, whereas the 33-section model experiences its largest stiffness increase at Step 4, with increases of 75% in bending and 74% in torsion. This behaviour arises from local thickness adjustments enabled by the finer discretisation when secondary structural components and inertial loads are introduced. These results indicate that composite sizing is primarily governed by global buckling constraints, whereas metallic sizing is more sensitive to local load distribution and design-region resolution.

The introduction of fatigue constraints at Steps 5–6 leads to further stiffening in both material systems, accompanied by reduced deflections and changes in elastic twist. These effects result from increased panel thickness required to resist cyclic stresses. Although comparable stiffness levels are achieved, the composite wings realise these enhancements at lower mass, consistent with their higher fatigue resistance observed in the mass sensitivity analysis.

At Step 7, the 2.0 g flap-down load case produces predominantly bending-driven deformation with minimal torsional response, while the rolling manoeuvre at Step 8 induces the largest elastic twist with comparatively small bending deflection. These deformation patterns reflect the aerodynamic characteristics of the respective manoeuvres and, being less severe than the critical 2.5-g condition, exert limited influence on final sizing and global stiffness trends.

Engine loads introduced at Step 9 have a limited effect on global deformation. When applied in combination with the 2.5-g load and all structural and aeroelastic constraints, the resulting deflection and twist distributions remain close to those obtained at Step 2. The required structural reinforcement is confined to a localised region around the engine attachment, with a significant portion of the load transmitted through the pylon. Consequently, while SLoT captures the dominant global stiffness trends at the preliminary design stage, accurate representation of engine-pylon load paths ultimately requires higher-fidelity finite element modelling in later design phases.

4.3. *Effects of load cases and constraints on flutter prediction*

Fig. 13 presents the predicted flutter speeds at sea level for all sized wing configurations, together with the percentage change relative to the baseline case (Step 1). All configurations satisfy the applicable airworthiness requirement, with flutter speeds exceeding the critical threshold of 212.75 m/s (corresponding to $1.15V_D$).

Flutter speed generally increases from Steps 1 to 4 as buckling constraints, inertial effects, secondary structure, and fuel loads are progressively introduced. These trends are consistent with the stiffness increases discussed previously, with buckling emerging as the dominant driver. For the refined 33-section composite wing, the introduction of buckling at Step 2 increases flutter speed by 79% relative to Step 1. The subsequent inclusion of inertial and secondary-structure effects in Steps 3 and 4 provides additional increases of approximately 10% and 5%, respectively, resulting in a total increase of 94%. Notably, the flutter speed of 307 m/s at Step 1 lies close to the airworthiness limit, whereas by Step 4 the structure achieves an 88% flutter margin with only a 7.6% increase in mass.

For the manoeuvre load cases (Steps 5–8), flutter speeds remain well above the critical threshold and exceed the Step 1 values by more than 50% for all models except the 7-section composite configuration, which exhibits only a 13% increase due to its coarse representation of the stiffness distribution. Overall, these manoeuvre load cases exert a relatively modest influence on aeroelastic stability, despite differences in mass and stiffness between the models.

In contrast, engine effects introduced at Step 9 have a more pronounced impact on flutter behaviour. Flutter speeds decrease substantially, even though Steps 2 and 9 impose identical structural constraints and yield nearly identical mass and static deformation under the 2.5-g loading condition. For example, the flutter speed of the 7-section composite wing decreases from 627.5 m/s at Step 2 to 298 m/s at Step 9, while the corresponding metallic wing decreases from 637.5 m/s to 379 m/s. Negative changes relative to Step 1 are also observed for the 7-section composite and dummyTXdummy– 33-section metallic configurations. This degradation arises because, within the SAIT flutter analysis, the engine is modelled as a concentrated lumped mass, which significantly reduces the natural frequencies of the critical aeroelastic modes.

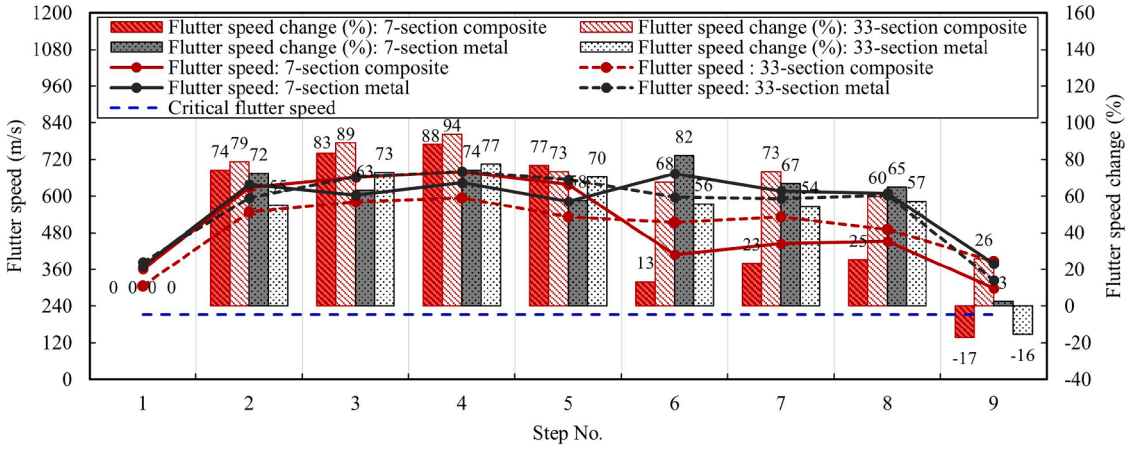


Fig. 13. Flutter speed at sea level with percentage changes for each model across the sensitivity analysis steps.

Table 7
Mode frequencies and flutter results at sea level of the 33-section composite and dummyTXdummy– metallic wing models at Step 9, with and without lumped engine mass.

Material	Cases	Mode 1 (Hz)	Mode 2 (Hz)	Mode 3 (Hz)	Mode 4 (Hz)	Mode 5 (Hz)	Flutter speed (m/s)	Flutter frequency (Hz)
Composite model	Clean-wing	2.88	10.88	23.85	43.80	76.49	548.50	51.30
	Engine-mass	2.88	10.88	23.79	36.49	44.65	386.25	37.30
Metallic model	Clean-wing	1.78	6.60	13.63	24.10	39.84	595.25	33.67
	Engine-mass	1.75	4.25	8.29	20.48	24.51	324.00	21.70

Table 7 compares the modal frequencies and flutter characteristics of the 33-section models with and without the inclusion of the lumped engine mass. The "clean-wing" configuration corresponds to the Step 9 sizing case, in which engine loads are considered during structural sizing, but the lumped engine mass is excluded from aeroelastic analysis. For the composite wing, inclusion of the engine mass reduces the frequencies of Modes 4 and 5 sufficiently to decrease the flutter frequency and flutter speed by 27.3% and 29.6%, respectively. For the metallic wing, the engine mass reduces the frequencies of all modes considered, resulting in a larger reduction in flutter speed of 45.6% relative to the clean-wing configuration. These results demonstrate that engine mass and placement must be explicitly and consistently represented in aeroelastic analysis and aerostructural optimisation. When engine effects are modelled appropriately, the SLoT-based sizing approach continues to yield wing designs that satisfy flutter requirements under the specified loading and constraint sets.

5. Case study of multidisciplinary optimisation of wing planform variations and data-driven design exploration

5.1. Design variables and dataset construction

The preceding sensitivity analysis examined the influence of load cases and structural constraints on sizing outcomes for the CRM baseline wing. Building on this workflow, the present case study modifies the wing planform to demonstrate the capability of the SLoT–SAIT toolset to size and assess wings with varying geometric inputs and design objectives at the preliminary design stage.

In this study, the aspect ratio (AR) and taper ratio (TR) are selected as the primary MDO variables, with the objective of minimising structural mass while satisfying strength, buckling, fatigue, and aeroelastic constraints. Ten wing configurations are generated with AR values ranging from 9 to 14 and are summarised in Table 8. Each configuration is defined by its planform parameters (AR, TR, and wingspan) together with the selected material system (composite or metallic).

To maintain computational efficiency while enabling meaningful geometric variation, the following modelling assumptions are adopted: (i) the number of ribs and their non-dimensional spanwise locations are retained from the original CRM planform; (ii) the non-dimensional location of the kink chord is fixed; and (iii) the wing planform area is held constant to preserve wing loading. As an illustration, Fig. 14 compares three metallic configurations: Cases 1 and 4 differ primarily in aspect ratio, while Cases 4 and 6 have similar aspect ratios but distinct taper ratios.

Table 8
Ten randomly generated design cases with varied wing planforms and material systems.

Case No.	AR	TR	Span (m)	Material
1	13.82	0.23	72.83	metal
2	11.32	0.19	65.91	composite
3	12.57	0.15	69.46	composite
4	10.07	0.25	62.17	metal
5	13.20	0.21	71.16	composite
6	10.70	0.17	64.07	metal
7	11.95	0.26	67.71	composite
8	9.45	0.22	60.21	composite
9	13.51	0.18	72.00	metal
10	11.01	0.24	65.00	composite

Sizing and analysis of all ten configurations are performed individually using the SLoT–SAIT workflow under the critical 2.5-g manoeuvre load and the design constraints described previously. For each configuration, the toolset computes the minimum structural mass, flutter speed, and static aeroelastic responses, including wing deflection and elastic twist. The resulting collection of geometric inputs and aerostructural outputs forms a dataset that is subsequently used for a data-driven wing design study, in which machine learning models are trained to predict structural mass and flutter speed across the design space.

5.2. SHAP analysis

Fig. 15 presents parity plots comparing SHAP-based surrogate predictions with the corresponding true values for structural mass and flutter speed. Leave-one-out (LOO) cross-validation is used to assess model

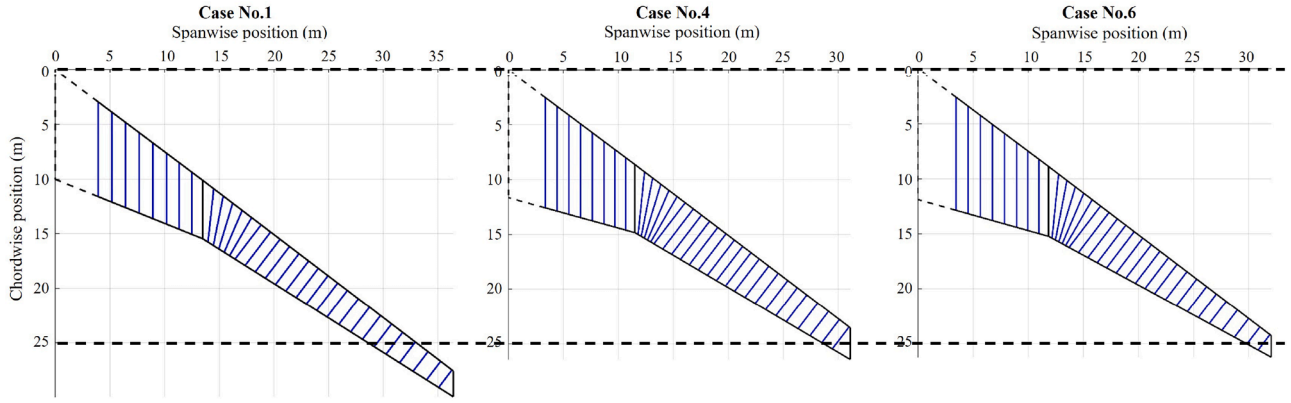


Fig. 14. Wing planform and rib layouts of Cases 1, 4, and 6.

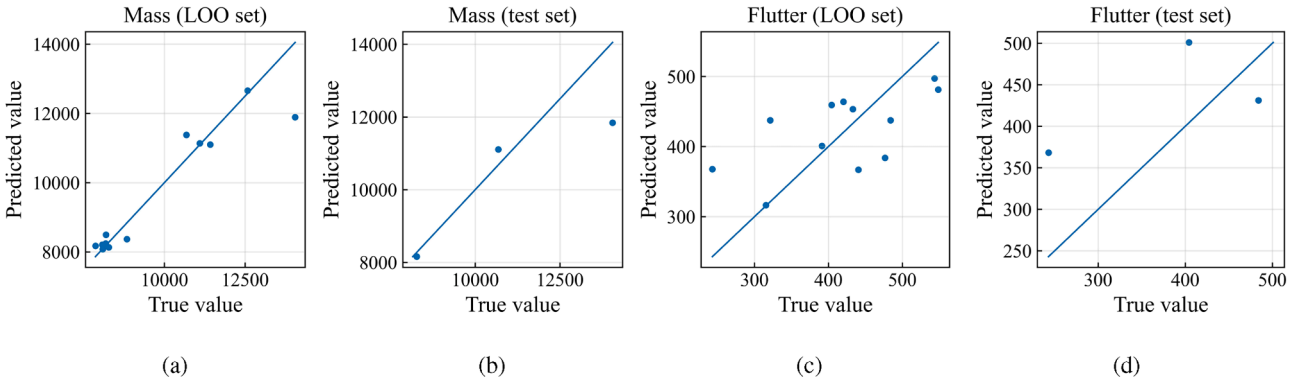


Fig. 15. Parity plots of RF predictions for wing mass (kg) and flutter speed (m/s).

robustness across the full dataset, while a separate test set evaluates generalisation to previously unseen configurations. For mass prediction, the results cluster closely around the 1:1 line for both the LOO and test sets, indicating small prediction errors and high surrogate fidelity. In contrast, flutter speed predictions exhibit greater scatter, reflecting the stronger nonlinearity of the aeroelastic response and the limited size of the available dataset. Nevertheless, the predictive accuracy remains sufficient for early-stage design exploration and, with additional training data, could support practical application when combined with an appropriate flutter-margin safety factor.

Fig. 16 presents the global SHAP summary plots for mass and flutter speed, illustrating both the relative importance of each feature and the direction of its influence. For structural mass, the material system is the dominant contributor: metallic configurations consistently exhibit positive SHAP values, corresponding to higher mass, whereas composite configurations yield negative SHAP values, indicating lower mass. Aspect ratio (AR) and wingspan also contribute positively to mass, while taper ratio (TR) shows a weaker and mildly nonlinear influence.

For flutter speed, AR and wingspan emerge as the most influential parameters. Increasing AR and span generally reduces flutter speed, as indicated by negative SHAP contributions. The material system plays a secondary role, with composite wings tending to exhibit slightly higher flutter speeds, while TR again exerts the weakest influence among the considered variables.

Overall, the SHAP analysis confirms that the surrogate model captures physically meaningful relationships and provides interpretable sensitivity information. This interpretability helps bridge data-driven modelling and engineering intuition by identifying dominant design drivers, revealing nonlinear interactions among variables, and informing future sampling strategies or optimisation efforts within the proposed data-driven wing design framework.

5.3. GPR predictions

As indicated by the SHAP analysis, the material system and aspect ratio (AR) are the dominant drivers of both structural mass and flutter behaviour. Accordingly, the Gaussian Process Regression (GPR) models are examined with respect to these two variables, comparing composite and metallic wings across the AR range using leave-one-out (LOO) predictions and their associated 95% prediction intervals, as shown in Fig. 17.

For structural mass (Fig. 17a), both the true values and the GPR mean predictions increase monotonically with AR for each material system. Metallic wings remain consistently heavier than composite wings across the entire AR range, and the corresponding 95% prediction intervals do not overlap, indicating a clear separation between the two material classes. Most LOO samples lie well within the predicted uncertainty bounds, demonstrating that the GPR model captures the dominant trend and provides a reliable estimate of predictive uncertainty. From a design perspective, the results indicate that the composite wing remains robustly lighter than its metallic counterpart throughout the examined AR range.

For flutter speed (Fig. 17b), the GPR mean predictions correctly reproduce the expected decrease in flutter speed with increasing AR. Composite wings exhibit higher flutter speeds than metallic wings at the same AR, with well-separated prediction intervals at low-to-moderate AR values. At the highest AR values, the prediction intervals increasingly overlap, reflecting greater uncertainty in regions where training data are sparse. Therefore, the widening uncertainty bounds at large AR identify regions where additional sampling would most effectively improve surrogate accuracy. In an uncertainty-aware design context, these prediction intervals enable designers to assess not only deterministic feasibility but also the robustness of

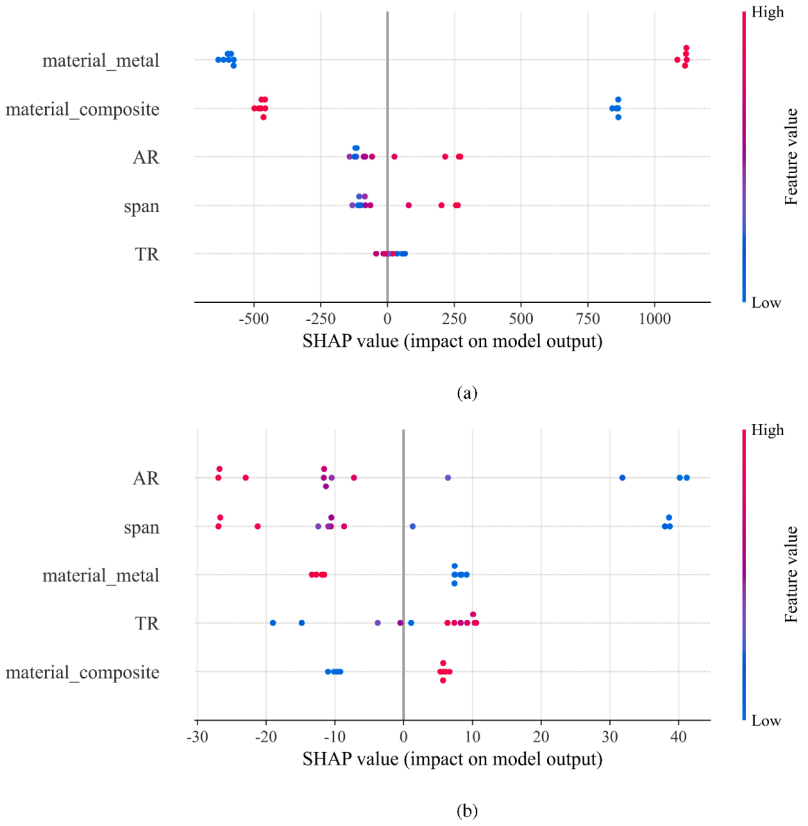


Fig. 16. Global SHAP summary for (a) mass and (b) flutter speed.

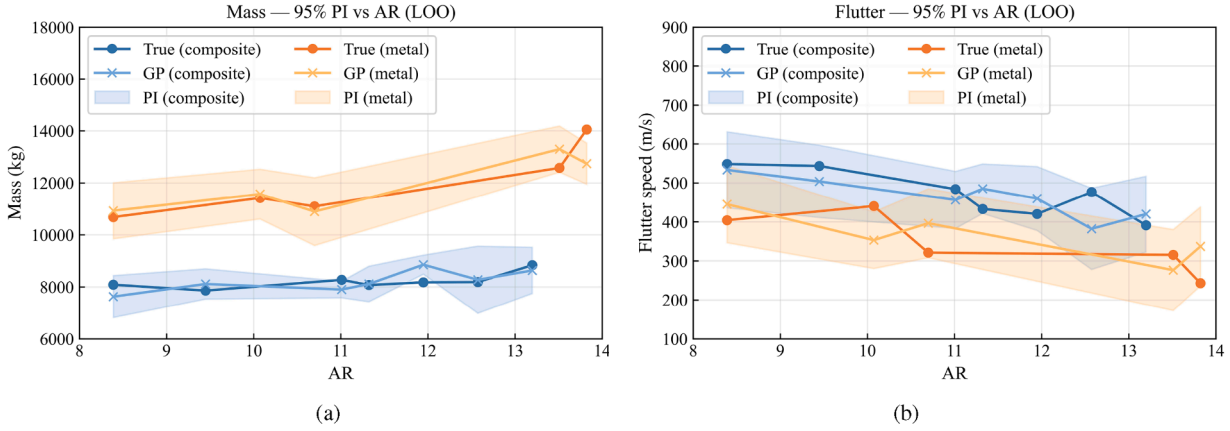


Fig. 17. GPR LOO predictions and 95% prediction intervals versus AR for (a) mass and (b) flutter speed, comparing composite and metallic wings.

candidate designs with respect to prescribed flutter-margin safety factors.

5.4. Inverse design results

Across both the deterministic and chance-constrained optimisation runs, the five lightest feasible solutions identified by the surrogate-based search correspond to composite wing configurations. This result indicates that, within the explored design space, composite structures consistently provide a more favourable mass-flutter trade-off than metallic wings. The corresponding inverse-designed configurations are summarised in Table 9.

A representative optimal design has an aspect ratio of AR= 9.68, a taper ratio of TR= 0.22, a wingspan of 60.34 m, and an estimated structural mass of 8011.41 kg. The predicted flutter speeds for this configuration are 523.85 m/s using the deterministic surrogate model and 532.78 m/s based on the GPR mean prediction. For the chance-constrained solutions, the 95% GPR lower confidence bound on flutter speed also exceeds the target requirement, indicating that these designs remain feasible when surrogate-model uncertainty is explicitly accounted for, rather than relying solely on mean predictions.

Direct comparisons between metallic and composite wings with identical planform geometries further highlight the advantages of composite construction. For the representative geometry (AR= 9.68), the metallic wing exhibits a minimum mass of 11 095.14 kg and predicted flutter speeds of 489.62 m/s using the deterministic surrogate, with a corresponding 95% lower confidence bound of 419.90 m/s. These results illustrate both the mass penalty and the reduced flutter margin associated with metallic designs for equivalent planform shapes.

Table 9
Top surrogate-based inverse design candidates under deterministic and chance-constrained flutter limits.

Feasible designs	Material	AR	TR	Span (m)	Mass (kg) - deterministic	Flutter speed (m/s) - deterministic	Flutter speed (m/s) - chance
1	composite	9.68	0.219	60.34	8011.41	523.85	532.79
2	composite	8.97	0.220	60.11	8011.41	532.83	532.83
3	composite	9.35	0.224	59.55	8011.41	524.45	539.97
4	composite	9.25	0.220	60.66	8011.41	517.08	528.51
5	composite	9.13	0.224	59.50	8011.41	532.83	545.40

While the present study demonstrates a proof-of-concept framework for rapid wing sizing and data-driven MDO, several limitations remain. The current dataset is intentionally small and restricted to a limited range of planform variations and load cases, which constrains surrogate accuracy, particularly for flutter prediction. In addition, certain structural layout parameters, such as rib number and location and kink chord position, were fixed in the present study to limit the design space and enable a computationally efficient demonstration. Within the proposed MDO framework, all such inputs can also be treated directly as design variables for future multi-objective design and sensitivity studies. Future work will therefore expand both the design space and the dataset to include broader geometric, material, and loading variations, as well as additional performance metrics such as fuel burn, efficiency, and operational margins. These extensions will support the development of more reliable and informative multi-objective surrogate models.

Further efforts will focus on improving GPR calibration for uncertainty quantification, refining SHAP-based sensitivity analysis through richer training datasets, and extending the inverse design capability to generate detailed thickness, stiffness, and mass distributions. Validation of the surrogate-based inverse design using the original physics-based structural solvers, together with verification against high-fidelity finite-element models, will further strengthen the proposed framework. In addition, the incorporation of a more comprehensive load envelope and tighter aeroelastic coupling will enhance its applicability to preliminary MDO and early-stage airworthiness assessment.

6. Conclusion

This paper presented an efficient and computationally rapid framework for preliminary wing sizing and aeroelastic analysis that integrates low- and medium-fidelity structural solvers (SLoT and SAIT) with aerodynamic models within an MDO context. The proposed workflow enables rapid sizing of composite and metallic wing boxes across multiple load cases, planform variations, material systems, and structural constraints, delivering detailed panel thickness distributions, sectional mass estimates, static aeroelastic responses, jig-shape indications, modal characteristics, and flutter predictions.

- **Model resolution:** Coarse (7-section) and fine (33-section) discretisations yield total mass estimates within $\sim 10\%$, but fine resolution is required to capture localised effects, particularly secondary structures and engine-induced loads, without distorting global trends.
- **Constraint drivers:** Buckling and fatigue are the dominant sizing constraints. Composite wings are driven primarily by buckling, whereas metallic wings are strongly influenced by fatigue and sectional load distributions.
- **Composite versus metallic:** Composite wings achieve roughly 30% lower mass than metallic wings while maintaining adequate aeroelastic margins.
- **Engine effects:** Concentrated engine mass substantially modifies mode shapes and frequencies, producing large changes in flutter speed; explicit engine modelling is therefore essential in aerostructural MDO.
- **Load-constraint coupling:** Realistic load cases combined with structural constraints significantly alter weight-performance trade-offs. Strength criteria under 2.5 g alone are insufficient; accounting for buckling, fatigue, secondary components, fuel, and realistic load distributions can increase mass by $\sim 8\%$ for composite and $\sim 55\%$ for metallic wings.

A parametric study of ten planform-material cases generated a dataset enabling a transition from deterministic sizing toward data-driven MDO. Random Forest surrogates reproduced mass and flutter trends with strong parity, and SHAP analysis provided interpretable, physics-consistent feature attributions: material type dominates both mass and flutter; increasing AR raises mass and lowers flutter speed; TR has weaker but nonlinear influences. Gaussian Process Regression added uncertainty awareness through two-sided 95% prediction intervals, distinguishing deterministically feasible from robustly feasible designs. Leave-one-out validation confirmed generalisation despite the limited dataset. Using these surrogates, inverse designs satisfying flutter constraints and minimising structural weight were identified rapidly.

Overall, the proposed multi-fidelity toolset combined with interpretable surrogate modelling enables rapid exploration of large wing design spaces with controlled accuracy and quantified uncertainty, effectively bridging physics-based sizing and data-driven prediction. The framework supports early-stage MDO trade studies, reduces reliance on manual load-case evaluation, and provides feature-level insight to guide design decisions. These results demonstrate a practical pathway toward scalable, uncertainty-aware, data-driven wing design methodologies suitable for next-generation aircraft development.

CRediT authorship contribution statement

Yingjun Pan: Writing – original draft, Validation, Software, Resources, Methodology, Investigation, Formal analysis, Data curation, Conceptualization; **Mushfiqul Alam:** Supervision, Project administration; **James Whidborne:** Supervision, Project administration; **Mark Westwood:** Project administration, Funding acquisition.

Data availability

Data will be made available on request.

Declaration of competing interest

The authors declare that they have no known competing financial interests or personal relationships that could have appeared to influence the work reported in this paper.

Acknowledgments

This research was supported by the Out of Cycle Next Generation Highly Efficient Air Transport (ONEheart) project funded through the UK Research and Innovation (UKRI10003388). The authors would like to thanks for the support and cooperation from the Airbus Operations Limited UK.

References

[1] Air Transport Action Group, Waypoint 2050: Balancing growth in connectivity with a comprehensive global air transport response to the climate emergency: a vision of net-zero aviation by mid-century, Technical Report, Air Transport Action Group (ATAG), 2021. Second edition.

[2] F. Collier, R. Thomas, C. Burley, C. Nickol, C.M. Lee, M. Tong, Environmentally responsible aviation - real solutions for environmental challenges facing aviation, in: 27th Congress of International Council of the Aeronautical Sciences, Nice, France, September 19–24, 2010.

[3] G.M. Bezos-O'Connor, M.F. Mangelsdorf, H.A. Maliska, A.E. Washburn, R.A. Wahls, Fuel efficiencies through airframe improvements, in: 3rd AIAA Atmospheric Space Environments Conference, Honolulu, Hawaii, June 27–30, 2011. https://doi.org/10.2514/6.2011-3530

[4] R.M. Ajaj, M.I. Friswell, D. Smith, A.T. Isikveren, A conceptual wing-box weight estimation model for transport aircraft, Aeronaut. J. 117 (1191) (2013) 533–551. https://doi.org/10.1017/S0001924000008174

[5] G. Bindolino, G. Ghiringhelli, S. Ricci, M. Terraneo, Multilevel structural optimization for preliminary wing-box weight estimation, J. Aircr. 47 (2) (2010) 475–489. https://doi.org/10.2514/1.41552

[6] T. Führer, C. Willberg, S. Freund, F. Heinecke, Automated model generation and sizing of aircraft structures, Aircr. Eng. Aerosp. Technol. 88 (2) (2016) 268–276. https://doi.org/10.1108/AEAT-02-2015-0054

[7] F. Hürlimann, R. Kelm, M. Dugas, K. Oltmann, G. Kress, Mass estimation of transport aircraft wingbox structures with a CAD/CAE-based multidisciplinary process, Aerosp. Sci. Technol. 15 (4) (2011) 323–333. https://doi.org/10.1016/j.ast.2010.08.005

[8] D. Li, J. Xiang, S. Guo, R. Xu, Optimization of composite wing structure for a flying wing aircraft subject to multi constraints, in: 54th AIAA/ASME/ASCE/AHS/ASC Structures, Structural Dynamics, and Materials Conference, Boston, Massachusetts, April 8–11, 2013. https://doi.org/10.2514/6.2013-1934

[9] A. Schuster, J. Scherer, T. Führer, T. Bach, D. Kohlgrüber, Automated sizing Process of a Complete Aircraft Structure for the Usage within a MDO Process, Deutsche Gesellschaft für Luft-und Raumfahrt-Lilienthal-Oberth eV, 2016.

[10] C. You, M. Yasaee, S. He, D. Yang, Y. Xu, I. Dayyani, H. Ghasemnejad, S. Guo, P. Webb, J. Jennings, G. Federico, Identification of the key design inputs for the FEM-based preliminary sizing and mass estimation of a civil aircraft wing box structure, Aerosp. Sci. Technol. 121 (107284) (2022). https://doi.org/10.1016/j.ast.2021.107284

[11] T.F. Wunderlich, S. Dähne, L. Reimer, A. Schuster, O. Brodersen, Global aerostructural design optimization of more flexible wings for commercial aircraft, in: AIAA Aviation 2020 Forum, 1 Part F, American Institute of Aeronautics and Astronautics Inc, AIAA, 2020, pp. 1–30. https://doi.org/10.2514/6.2020-3170

[12] P.D. Ciampa, B. Nagel, M. Van Tooren, Global local structural optimization of transportation aircraft wings, Collection of Technical Papers - AIAA/ASME/ASCE/AHS/ASC Structures, Structural Dynamics and Materials Conference (2010). https://doi.org/10.2514/6.2010-3098

[13] S. Grihon, L. Krog, D. Bassir, Numerical optimization applied to structure sizing at AIRBUS: a multi-step process, Int. J. Simul. Multi. Des. Optim. 3 (4) (2009) 432–442. https://doi.org/10.1051/ijsmdo/2009020

[14] S. Grihon, P. Kaletta, Rapid sizing for conceptual design at AIRBUS, in: Proceedings of the Airbus Conference, Airbus and SAMTECH, Liège, Belgique, 3, 2009.

[15] L. Iorga, V. Malmedy, O. Stodieck, S. Coggon, J. Loxham, Preliminary sizing optimisation of aircraft structures: industrial challenges and practices, in: 6th Aircraft Structural Design Conference, Bristol, Sep 20, 2018.

[16] S.L. Brunton, J.N. Kutz, K. Manohar, A.Y. Aravkin, K. Morgansen, J. Klemisch, N. Goebel, J. Buttrick, J. Poskin, A.W. Blom-Schieber, T. Hogan, D. McDonald, Data-driven aerospace engineering: reframing the industry with machine learning, AIAA J. 59 (8) (2021) 2820–2847. https://doi.org/10.2514/1.J060131

[17] A.C. Gray, C. Riso, E. Jonsson, J.R.R.A. Martins, C.E.S. Cesnik, High-Fidelity aerostructural optimization with a geometrically nonlinear flutter constraint, AIAA J. 61 (6) (2023) 2430–2443. https://doi.org/10.2514/1.J062127

[18] J.T. Hwang, A. Ning, Large-scale multidisciplinary optimization of an electric aircraft for on-demand mobility, booktitleAIAA/ASCE/AHS/ASC Structures, Structural Dynamics, and Materials Conference (2018) 1–18. https://doi.org/10.2514/6.2018-1384

[19] O. Dababneh, T. Kipouros, J.F. Whidborne, Multidisciplinary design optimization of the NASA metallic and composite common research model wingbox: addressing static strength, stiffness, aeroelastic, and manufacturing constraints, Aerospace 12 (6) (2025). https://doi.org/10.3390/aerospace12060476

[20] Y. Zhang, D. Jia, E.K. Bontoft, V. Toropov, Wing jig shape optimisation with gradient-assisted metamodel building in a trust-region optimisation framework, Struct. Multidiscip. Optim. 65 (12) (2022). https://doi.org/10.1007/s00158-022-03453-0

[21] N. Kroll, D. Dimitrov, T. Franz, T. Führer, T. Gerhold, S. Langer, D. Liu, R. Liepelt, L. Reimer, M. Ritter, A. Schwöppe, J. Scherer, DLR Projekt digital-X: auf dem weg zur virtuellen flugzeugentwicklung und flugerprobung auf basis höherwertiger verfahren, in: Deutscher Luft- Und Raumfahrtkongress, Augsburg, Sep 16–18, 2014.

[22] G.K.W. Kenway, J.R.R.A. Martins, Multipoint high-fidelity aerostructural optimization of a transport aircraft configuration, J. Aircr. 51 (1) (2014) 144–160. https://doi.org/10.2514/1.C032150

[23] S. Mohaghegh, A. Mohaghegh, Machine learning in aircraft design: a comprehensive review of optimization, aerodynamics, and structural applications, IEEE Access 13 (2025) 105642–105653. https://doi.org/10.1109/ACCESS.2025.3580485

[24] J. Li, S. He, J.R.R.A. Martins, Data-driven constraint approach to ensure low-speed performance in transonic aerodynamic shape optimization, Aerosp. Sci. Technol. 92 (2019) 536–550. https://doi.org/10.1016/j.ast.2019.06.008

[25] K. Zheng, Y. Wang, F. Liu, Q. Zhang, W. Song, CST-LLM: Enhancing airfoil parameterization method with large language model, Aerosp. Sci. Technol. 166 (July) (2025) 110548. https://doi.org/10.1016/j.ast.2025.110548

[26] P.C. Verpoort, P. MacDonald, G.J. Conduit, Materials data validation and imputation with an artificial neural network, Comput. Mater. Sci 147 (2018) 176–185. https://doi.org/10.1016/j.commatsci.2018.02.002

[27] B.D. Conduit, N.G. Jones, H.J. Stone, G.J. Conduit, Probabilistic design of a molybdenum-base alloy using a neural network, Scr Mater. 146 (2018) 82–86. https://doi.org/10.1016/j.scriptamat.2017.11.008

[28] R. Zhao, R. Yan, Z. Chen, K. Mao, P. Wang, R.X. Gao, Deep learning and its applications to machine health monitoring, Mech. Syst. Signal Process. 115 (2019) 213–237. https://doi.org/10.1016/j.ymssp.2018.05.050

[29] B. Eroglu, M.C. Sahin, N.K. Ure, Autolanding control system design with deep learning based fault estimation, Aerosp. Sci. Technol. 102 (2020) 105855. https://doi.org/10.1016/j.ast.2020.105855

[30] U.J. Ravaioli, J. Cunningham, J. McCarroll, V. Gangal, K. Dunlap, K.L. Hobbs, Safe reinforcement learning benchmark environments for aerospace control systems, in: 2022 IEEE Aerospace Conference (AERO), Big Sky, MT, USA, 2022, pp. 1–20. https://doi.org/10.1109/AERO53065.2022.9843750

[31] Y. Tong, M. Luo, S. Ren, Z. Zhang, C. Xing, Z. Du, A rapidly structured aircraft concept design method based on generative artificial intelligence, Chin. J. Aeronaut. 38 (10) (2025) 103629. https://doi.org/10.1016/j.cja.2025.103629

[32] M. Hasan, A. Khandoker, G. Gessl, M.A. Hamid, M. Ali, Low fidelity data driven machine learning based optimisation method for box-wing configuration, Aerosp. Sci. Technol. 150 (2024) 109169. https://doi.org/10.1016/j.ast.2024.109169

[33] Y. Pan, M. Alam, A. Spinelli, E.B. Aldana, Structural and aeroelastic optimization of a large aircraft wing with a passive twist wingtip, in: ICAS Proceedings 34th Congress of the International Council of the Aeronautical Sciences, Florence, Italy, Sep, 2024.

[34] E.S. D.U. (ESDU), ESDU 95010 Computer program for estimation of spanwise loading of wings with camber and twist in subsonic attached flow effect of plain flaps, 1999.

[35] E.S. D.U. (ESDU), ESDU 083040 Method for the rapid estimation of spanwise loading of wings with camber and twist in subsonic attached flow, Technical Report, HIS ESDU: London, UK, 2013.

[36] S.A. Prince, D. Di Pasquale, K. Garry, C. Nuzzo, A rapid aerodynamic prediction method for unconventional transonic aircraft configurations, in: 31st Congress of International Council of the Aeronautical Sciences, Belo Horizonte, Brazil, 2018.

[37] D. Mark, Y. Harold, Athena Vortex Lattice (AVL), 2023. Aerodynamic and flight-dynamic analysis software.

[38] T.H.G. Megson, Aircraft Structures for Engineering Students, Elsevier, 2012.

[39] L.P. Kollar, G.S. Springer, Mechanics of Composite Structures, Cambridge university press, 2003.

[40] E.A. Armanios, A.M. Badir, Free vibration analysis of anisotropic thin-walled closed-section beams, AIAA J. 33 (10) (1995) 1905–1910. https://doi.org/10.2514/3.12744

[41] S. Guo, Aeroelastic optimization of an aerobatic aircraft wing structure, Aerosp. Sci. Technol. 11 (5) (2007) 396–404.

[42] J.R. Banerjee, F.W. Williams, Free vibration of composite beams-an exact method using symbolic computation, J. Aircr. 32 (3) (1995) 636–642. https://doi.org/10.2514/3.46767

[43] J.R. Banerjee, F.W. Williams, Coupled bending-torsional dynamic stiffness matrix for Timoshenko beam elements, Comput. Struct. 42 (3) (1992) 301–310. https://doi.org/10.1016/0045-7949(92)90026-V

[44] M.C.-Y. Niu, Airframe Structural Design : Practical Design Information and Data on Aircraft Structures, Conmilit Press, Hong Kong, Hong Kong, 1999.

[45] E.S. D.U. (ESDU), ESDU 03001 Elastic buckling of long, flat, symmetrically-laminated (AsBoDf), composite stiffened panels and struts in compression, Technical Report, HIS ESDU: London, UK, 2003.

[46] S. Song, H. Zang, N. Duan, J. Jiang, Experimental research and analysis on fatigue life of carbon fiber reinforced polymer (CFRP) tendons, Mater. (Basel) 12 (20) (2019). https://doi.org/10.3390/ma12203383

[47] N. Morita, Y. Mino, N. Yoshikawa, M. Hojo, Versatile fatigue strength evaluation of unidirectional CFRP specimen based on micro-stress analysis of resin, Compos. Struct. 276 (December 2020) (2021) 114539. https://doi.org/10.1016/j.compstruct.2021.114539

[48] NASA Langley Research Center, Common Research Model (CRM) Wingbox Finite Element Models: Wingbox Models Description, 2014.

[49] The MathWorks, Inc., fminunc: Find minimum of unconstrained multivariable function, The MathWorks, Inc., Natick, Massachusetts, United States.

[50] S.M. Lundberg, S.-i. Lee, A unified approach to interpreting model predictions, in: 31st Conference on Neural Information Processing Systems (NIPS 2017), Long Beach, CA, USA. 2017, pp. 1–10.

[51] H. Chen, I.C. Covert, S.M. Lundberg, S.-i. Lee, Algorithms to estimate shapley value feature attributions, Nat. Mach. Intell. 5 (December 2020) (2023) 590–601. https://doi.org/10.1038/s42256-023-00657-x

[52] B. Rozemberczki, L. Watson, P. Bayer, H.-T. Yang, O. Kiss, S. Nilsson, R. Sarkar, The shapley value in machine learning, in: L. De Raedt (Ed.), Proceedings of the Thirty-First International Joint Conference on Artificial Intelligence, IJCAI-22, International Joint Conferences on Artificial Intelligence Organization, Vienna, Austria. 2022, pp. 5572–5579. https://doi.org/10.24963/ijcai.2022/778

[53] L. Breiman, Random forests, Mach. Learn. 45 (2001) 5–32. https://doi.org/10.1023/A:1010933404324

[54] T. Chen, C. Guestrin, XGBoost: A scalable tree boosting system, in: Proceedings of the 22nd ACM SIGKDD International Conference on Knowledge Discovery and Data Mining, KDD '16, Association for Computing Machinery, New York, NY, USA, 2016, p. 785-794. https://doi.org/10.1145/2939672.2939785

[55] S.M. Lundberg, G. Erion, H. Chen, A. DeGrave, J.M. Prutkin, B. Nair, R. Katz, J. Himmelfarb, N. Bansal, S.-I. Lee, From local explanations to global understanding

with explainable AI for trees, Nat. Mach. Intell. 2 (1) (2020) 56–67. https://doi.org/10.1038/s42256-019-0138-9
[56] C.E. Rasmussen, C.K.I. Williams, Gaussian Processes for Machine Learning, 2, Massachusetts Institute of Technology, 2006.
[57] I. Kavrakov, A. McRobie, G. Morgenthal, Data-driven aerodynamic analysis of structures using gaussian processes, J. Wind Eng. Ind. Aerodyn. 222 (2022). https://doi.org/10.1016/j.jweia.2022.104911
[58] F. Pedregosa, G. Varoquaux, A. Gramfort, V. Michel, B. Thirion, O. Grisel, M. Blondel, P. Prettenhofer, R. Weiss, V. Dubourg, et al., Scikit-learn: machine learning in Python, J. Mach. Learn. Res. 12 (2011) 2825–2830.
[59] D.C. Montgomery, G.C. Runger, Applied Statistics and Probability for Engineers, John wiley & sons, 2010.
[60] C.P. Robert, G. Casella, G. Casella, Monte Carlo Statistical Methods, 2, Springer, 1999.
[61] J. Bergstra, Y. Bengio, Random search for hyper-parameter optimization, J. Mach. Learn. Res. 13 (1) (2012) 281–305.
[62] J. Vassberg, M. Dehaan, M. Rivers, R. Wahls, Development of a common research model for applied CFD validation studies, in: 26th AIAA Applied Aerodynamics Conference, H, Hawaii, 2008. https://doi.org/10.2514/6.2008-6919
[63] Z. Lyu, J.R.R.A. Martins, Aerodynamic design optimization studies of a blended-wing-body aircraft, J. Aircr. 51 (5) (2014) 1604–1617. https://doi.org/10.2514/1.C032491
[64] D. Hue, F. Sartor, I. Petropoulos, C. Fournis, DPW-7: Steady and unsteady computations of the common research model at different reynolds numbers, J. Aircr. 60 (6) (2023) 1857–1871. https://doi.org/10.2514/1.C037231
[65] T.R. Brooks, G.K.W. Kenway, J.R.R.A. Martins, Undeflected common research model (uCRM): an aerostructural model for the study of high aspect ratio transport aircraft wings, in: 35th AIAA Applied Aerodynamics Conference, 2017, American Institute of Aeronautics and Astronautics Inc, AIAA, Denver, Colorado, June, 2017. https://doi.org/10.2514/6.2017-4456
[66] E. Torenbeek, Development and Application of a Comprehensive, Design-sensitive Weight Predicition Method for Wing Structures of Transport Category Aircraft, 1992.



https://dspace.org/

Rapid preliminary aircraft wing sizing for metallic and composite structures to support data-driven multidisciplinary design optimisation frameworks

Pan, Yingjun; Alam, Mushfiqul; Whidborne, James F.; Westwood, Mark

2026-10
Elsevier
https://doi.org/10.1016/j.ast.2026.112250
Pan Y, Alam M, Whidborne J, Westwood M. (2026) Rapid preliminary aircraft wing sizing for metallic and composite structures to support data-driven multidisciplinary design optimisation frameworks. Aerospace Science and Technology, Volume 177, Part A, October 2026, Article number 112250

Downloaded from a DSpace repository. https://dspace.org/